4-2014

Simulation of an Intake Manifold Pre-Heater for Cold Diesel Engine Startup

Patrick K. Kreun
Western Michigan University, patrick.k.kreun@wmich.edu

Recommended Citation
Kreun, Patrick K., "Simulation of an Intake Manifold Pre-Heater for Cold Diesel Engine Startup" (2014). *Master's Theses*. 475.
http://scholarworks.wmich.edu/masters_theses/475

SIMULATION OF AN INTAKE MANIFOLD PRE-HEATER FOR COLD DIESEL ENGINE STARTUP

by

Patrick K. Kreun

A thesis submitted to the Graduate College
in partial fulfillment of the requirements
for the degree of Master of Science in Engineering (Mechanical)
Mechanical and Aerospace Engineering Department
Western Michigan University
April 2014

Thesis Committee:

Claudia M. Fajardo-Hansford, Ph.D., Chair
William W. Liou, Ph.D.
Christopher Cho, Ph.D.

SIMULATION OF AN INTAKE MANIFOLD PRE-HEATER FOR COLD DIESEL ENGINE STARTUP

Patrick K. Kreun, M.S.E.

Western Michigan University, 2014

Ensuring consistent, reliable diesel engine startups in cold temperatures is of utmost importance in a number of applications. Under extreme temperatures, the use of glow plugs is complemented by intake manifold heaters. In these, the energy released from combustion increases the intake air temperature before the air enters the main combustion chamber. Since the process also alters the stoichiometry of the fuel-air mixture at the intake ports, the pre-heater operation must be optimized in order to guarantee successful and reliable in-cylinder combustion during engine startups. This paper describes the development of an intake manifold model incorporating an air pre-heater for application in a diesel engine. The model, created using a commercial one-dimensional simulation tool, was validated against experimental data and subsequently used to quantify the concentration of combustion product species at the intake runners, as well as intake charge dilution. Results showed that the effective equivalence ratio might increase up to 2.6 after the first 25 seconds of cranking, with 12.5% reduction of the O_2 concentration in the intake charge. These results led to the construction of a parametric study used to optimize heater operation. This study demonstrated that careful control of the pre-heater fuel delivery could yield favorable intake charge temperatures while reducing the total fuel usage and disruption of air-fuel stoichiometry.

ACKNOWLEDGEMENTS

I would like to start by thanking my graduate advisor, Dr. Claudia Fajardo-Hansford, for her tireless efforts in support of this work. Without her continued guidance and motivation I am certain this thesis would simply be a tortuous collection of modeling data rather than the document presented now. I would also like to extend my gratitude to everyone in my department who has helped bring this work to fruition, particularly my committee members and the Center for Advanced Vehicle Design and Simulation (CAViDS).

A very special thank you goes out to L3 Communications for making this work possible through both funding and contribution of experimental test data; specifically, I would like to acknowledge Andreas Baumann and Dan Smith. Ryan Dudgeon and the entire Gamma Technologies support staff has been a tremendous resource as well. Without their direction whilst stumbling through the outer reaches of GT-POWER’s capabilities, this endeavor would have been destined to fail.

Finally, I would like to thank my friends and family for their continuing love, support, and encouragement, and most importantly my girlfriend, Alyssa, for her patience and understanding. To think, all those lonely nights amounted to this pile of ones and zeros.

Patrick K. Kreun

TABLE OF CONTENTS

ACKNOWLEDGEMENTS ii

LIST OF TABLES vii

LIST OF FIGURES.. viii

Chapter 1: INTRODUCTION 1

- 1.1 BACKGROUND 1
- 1.2 PRIOR RESEARCH ON DIESEL ENGINE COLD-START.. 2
- 1.3 PROBLEM DESCRIPTION AND MOTIVATION 5
- 1.4 GOALS AND OBJECTIVES.. 6
- 1.5 SUMMARY OF THESIS 7

Chapter 2: PHYSICAL SYSTEM 8

- 2.1 ENGINE 8
- 2.2 FLAME HEATER 9
- 2.3 EXPERIMENTAL SETUP 10

Chapter 3: MODEL DEVELOPMENT 12

- 3.1 MODELING SOFTWARE.. 12
  - 3.1.1 NUMERICAL METHOD 12
  - 3.1.2 DISCRETIZATION 13
  - 3.1.3 COMPONENT MODELING 16

Table of Contents - continued

Chapter 3: MODEL DEVELOPMENT

3.2 ASSUMPTIONS 16

3.3 GEOMETRY 19

3.4 MATERIALS 21

3.5 JP-8 22

3.6 FLAME HEATER MODELING 24

3.7 MODEL INSTABILITY 27

3.8 FLAME-HEATER VALIDATION 33

3.9 HEAT TRANSFER DISAGREEMENT 37

3.10 HEAT TRANSFER MODEL ALTERATION 41

Chapter 4: RESULTS 47

4.1 TEMPERATURE RESULTS 47

4.2 STOICHIOMETRY 49

4.3 FUEL CONSUMPTION 54

4.4 PARAMETRIC STUDY 55

Chapter 5: CONCLUSIONS AND FUTURE WORK 61

5.1 CONCLUSIONS 61

5.2 FUTURE WORK 62

BIBLIOGRAPHY 65

Table of Contents - continued

APPENDIX A: PARAMETRIC STUDY CASE SUMMARY.. 67

APPENDIX B: INTAKE RUNNER GAS COMPOSITION RESULTS FOR PARAMETRIC STUDY........ 68

APPENDIX C: SCRIPT FOR CALCULATING NOZZLE FLOW RATE.. 109

LIST OF TABLES

1: 1790 c.i. diesel engine specifications 8

2: Materials used during intake system modeling 21

3: Relevant properties of aviation fuel JP-8 22

4: Chemical and thermodynamic properties of JP-8 23

5: Transport properties of JP-8 24

6: General test conditions employed during stability study 27

7: Selected cases from stability study chosen to highlight results 28

8: Updated heat transfer correlation with necessary x/D values 43

9: Implementation of Nusselt number correction 45

10: Average and peak error of predicted intake runner gas temperatures with improved heat transfer model 47

11: Predicted chemical species concentrations at the flame heater outlet 50

12: JP-8 flammability limits 51

LIST OF FIGURES

1: Schematic of flame-heater and thermocouple locations..11

2: Illustration of 1-dimensional discretization strategy 14

3: Kearney et al., results of pulsatile flow [14]...18

4: Schematic of flame-heater model with corresponding GT-POWER objects...........................20

5: Schematic of intake manifold showing general layout 21

6a-6h: Instantaneous flame-heater gas temperatures from stability study...............................29

7: Predicted mass flow rate through flame-heater without PID control loop 31

8: Predicted mass flow rate through flame-heater with addition of PID control loop 32

9: Predicted mass flow rate through flame-heater with PID loop and redefined intake flow profile..33

10: Schematic of thermocouple location in relation to flame-heater orientation...................... 34

11: Predicted flame-heater outlet gas temperatures compared with experimentally measured values for initial test. Simulated results presented before the addition of a thermocouple object. 35

12: Predicted flame-heater outlet gas temperatures compared with experimentally measured values after implementation of equation 17. Simulated results presented before the addition of a thermocouple object..37

13: Intake runner gas temperature comparison between model predicted and experimentally measured results 38

14: Temperature response of *ThermalMass* object connected to intake runner 2 40

15: Runner 2 gas temperature results comparison. 42

16: Schematic of intake manifold with labeled flow components corresponding to Table 8 47

17: Comparison between default and improved heat transfer models in relation to experimentally measured intake runner 2 gas temperatures....................................46

List of Figures - continued

18: Comparison of predicted and experimental intake runner gas temperatures....................... 48

19: Error analysis of predicted intake gas temperatures with improved heat transfer model 49

20: Mole fraction of O2 needed to maintain constant charge mass-to-fuel mass ratio as the CSP mole fraction increases. Fuel: JP-8, Intake charge mass-to-fuel mass ratio =20.8 calculated with air dilution.. 53

21: Flame-heater fuel mass flow rate profile for selected frequency and duty cycles 56

22: Graphical representation of parametric study results... 57

23: Intake runner gas temperature comparison... 59

Chapter 1: INTRODUCTION

1.1 BACKGROUND

Internal combustion engines are required to operate consistently and reliably in a continually expanding range of conditions. And, as in any combustion-powered engine, their performance is inevitably tied to the combustion process. In diesel engines, the combustion process is broadly divided into four phases: the ignition delay, which is the period between start of fuel injection and the onset of combustion; the premixed combustion phase, during which the premixed portion of the fuel air mixture burns, leading to a rapid rate of heat release; the mixing-controlled phase, dominated by the rate at which the fuel-air mixture becomes available; and the late combustion phase, which may continue well into the expansion stroke as heat is released at a slower rate [1]. Each of these phases may be of particular interest to investigators; however, study of the ignition delay and premixed combustion phases are of distinct importance while researching diesel engine startability.

In a number of applications, diesel engines are required to start at sub-freezing ambient temperatures. Diesel engine cold-start can be regarded as a two-phase (albeit continuous) process. The first phase spans between the starter-on time and the time of first firing. In this phase, cold temperatures inhibit auto-ignition due to the reduction of combustion chamber temperatures, but also as a result of decreased in-cylinder pressures, reduced fuel pumpability, and higher oil viscosity. The second phase encompasses the period from first firing to stable idling. In this phase, combustion instabilities often manifest in the form of misfires and continue until the engine reaches a consistent idling speed. Here, cyclical variability, as well as the factors mentioned previously, can play an important role in determining cold start success. Failure to complete either phase results in an unsuccessful engine start attempt, the drawbacks of which include significant white smoke emissions, potentially higher operating costs, as well as the associated risk to personnel who may be dependent on reliable operation. This is a well founded concern, for example, in situations where diesel engines are employed in power generation, or in many military applications. To combat these issues, researchers have focused their efforts on gaining a greater understanding of the auto-ignition process and testing a variety of cold-start aids.

1.2 PRIOR RESEARCH ON DIESEL ENGINE COLD-START

Successful diesel engine cold-starts appear to rely on a delicate balance between heat transfer and auto ignition reaction timescales, at least until a threshold cranking speed is reached [2]. Paramount to the problem is the exponential dependence of ignition delay on combustion chamber temperatures, shown in equation 1.

$$\tau_{id} = AP^{-n} \exp(E_a /(RT)) \qquad (1)$$

where,

τ_{id}	Ignition delay (seconds)
A	Constant
P	Pressure
E_a	Apparent activation energy
R	Universal gas constant
T	Temperature

The compression temperature, which affects both physical and chemical delays, depends on external factors (e.g., ambient temperature) as well as on parameters related to engine design (e.g., compression ratio), and system design (e.g., cranking speed). From one perspective, higher cranking speeds are desirable to reduce the physical time available for heat and blowby losses. The consequently higher combustion chamber temperatures and pressures are desirable to reduce the ignition delay (see equation 1). On the other hand, higher cranking speeds lessen the physical time available for auto ignition reactions and might, therefore, hinder the starting process. At low temperatures, cranking speeds are typically low because the cranking load increases due to higher oil viscosity and diminished battery performance. The timescale balance previously described might, therefore, play a significant role during diesel engine cold-starts. Conventional diesel engines are typically equipped with glow plugs for cold-start assist. These are resistance heating elements placed in close proximity to the injector. Glow plugs assist with "hot spot" auto ignition by promoting rapid evaporation of the fuel in a localized area [1]. Medium to large diesel engines require additional start assist at subzero temperatures. Under these conditions, the most effective cold assist systems are coolant and intake air heaters. Researchers have also argued for the need of fuel heaters [3] and fuel filter heaters [4] at very low temperatures on the basis of fuel pumpability. Oil heaters, while effective in increasing cranking speed through a reduction in the oil viscosity, are generally not used as standalone systems [5] because they are less effective than coolant heaters in warming the engine as a whole. Hence, these and fuel heaters are complemented with alternative preheating devices. Solstad [4] and Sukala and Deckard [6] discussed the use of in-block immersion heaters and external heaters as a means to pre-warm the coolant. The warmer coolant circulates and heats up the engine to reduce heat loss during low-temperature cranking. The implementation of off-vehicle coolant-heating units, mainly for application in fleet vehicles, has also been discussed. These work either by directly exchanging warm coolant with a warmed up engine [5] or by using a central heating unit (e.g., boiler) and a heat exchanger system to preheat the coolant of the cold engine [4,6]. Practical drawbacks of the latter system include high installation costs, the need for fleet vehicles to depart from a common location, and the time required to preheat the coolant, which might take up to a few hours.

Intake manifold heaters, both electric and of the burner type, have also been used for cold-start assist of diesel engines with the goal of globally raising the intake air temperature. Electric manifold heaters consist of coil elements which through Joule heating increase the temperature of the intake air. Hakansson et. al. investigated the application of 1.8 kW to 4 kW electric intake air heaters for cold-start assist. The heater power output range was intended for engines with volumetric displacements ranging between 5.5 L and 16 L [7]. The use of the air pre-heater, combined with an in-house developed exhaust pressure governor and associated control system, proved effective at starting the engine after five seconds of cranking at -20°C ambient temperature. Payri et al. investigated the potential of using an electric intake manifold heater instead of glow plugs for starting a small, 1.4 L diesel engine at -20°C. For the same input energy and similar start duration, engine speed stability improved from ±70 RPM to ±6 RPM by the use of the manifold heater, while reducing HC and CO emissions [8].

The use of flame or burner heaters has not been widely discussed in the technical literature. Zheng et al. mention the use of a “small fuel burner” as a starting aid, but the work rather focuses on a coolant-type heater [5]. Lindl and Schmitz conducted an experimental investigation to compare the effectiveness of glow plugs, manifold electric heaters, and manifold flame heaters on diesel engine cold-start, based on the criteria of time to achieve a stable idling speed and amount of hydrocarbon emissions. They found similar performance with either type of manifold air heater [9]. Isley presented results of startup tests at subzero temperatures using a diesel-fueled compression ignition engine with and without a manifold flame heater [10]. Cold start times were reduced from 40 to 5 seconds at -25°C by using the flame heater.

Since manifold flame heaters are placed in the intake air path, their operation should be optimized such that the temperature of the intake charge is sufficiently raised, while maintaining high-enough downstream oxygen concentrations to sustain combustion in the main chamber. The operation of flame heaters during engine startups will significantly impact the effective air-fuel ratio at startup and the degree of dilution of the intake charge, both of which will strongly affect engine cold-start. The sustained use of flame heaters in a number of applications demands more detailed studies on their operation and influence on engine startability.

1.3 PROBLEM DESCRIPTION AND MOTIVATION

As discussed above, flame-heaters have been proven to be effective starting aids for diesel engines operating at subzero temperatures. However, the current state of research on these devices is somewhat limited. Since they generate heat by combusting fuel in the intake system of the engine, a portion of the oxygen normally reserved for combustion in the cylinders is burned. Because of this, it is imperative to balance the amount of heat released from combustion with the amount of oxygen consumed to provide the most favorable combination of intake gas temperature and gas composition to support auto-ignition.

Studies into the efficacy of flame-heaters as diesel starting aids have historically focused on experimental testing. While this type of investigation provides perhaps the most indisputable results, experimental testing can be quite expensive, particularly in the case of cold-start studies where testing must be performed in a climate controlled environment. This type of testing is also limited in the quantities that can be directly measured without disturbing the dynamics of the physical system. To combat these limitations, numerical modeling represents an attractive option.

This project represents one of the first published attempts to numerically model the intake system of a diesel engine incorporating a flame-heater.

1.4 GOALS AND OBJECTIVES

This goal of this research is to investigate the use of a flame heater for cold-start assist of a large, real-world diesel engine. Ultimately, it is desired to improve the diesel engine cold-start success rate, preferably by flame heater optimization and with minimum modifications to any of the engine subsystems used in the cold-start process. The following objectives were established in pursuit of this goal:

1. **Develop a numerical model of the intake system using a commercially available software package.**

   A numerical modeling approach was selected to provide a generous amount of flexibility while offering significant cost savings over traditional experimental means. Gamma Technologies' GT-SUITE was chosen for this purpose because of its availability and widespread use in industry settings, as well as to enable the integration of the present model with other existing models of the same engine. The one-dimensional modeling environment of this package is also advantageous in that it allows simulations to be run with greatly reduced computational expense when compared with three-dimensional modeling suites.

2. **Validate the intake system model incorporating the flame heater.**

   For a model to generate any justifiable results, it must be properly validated to ensure it accurately represents the physical system being simulated. The intake system model was, therefore, validated with experimental data measured from the physical system. The experimental setup used to gather these data, as well as the validation procedures will be discussed in section 3.8

3. **Quantify fuel usage, gas temperatures, gas composition, and intake charge dilution.** Once validated, the model was used to quantify the above parameters both directly downstream of the flame heater, as well as at each intake runner. Flame-heater fuel consumption, intake gas temperatures and composition, and intake charge dilution were selected due to their direct impact on auto-ignition and engine startability. It also should be noted that these are the main variables affected by modulation of the flame heater operation.

1.5 SUMMARY OF THESIS

The following describes the general structure of this thesis as well as a brief overview of each chapter:

Chapter 2 describes everything related to the physical engine that was modeled. Some general information about the engine is given first, followed by a detailed explanation of the flame-heater and its operation. Also covered is the test setup that was used to gather experimental data for development and comparison of the numerical model.

The modeling process is detailed in Chapter 3 starting with an overview of the software package used. Following this, the actual process of developing a numerical model is explained including assumptions made, geometrical constrains, material selections, and combustion modeling. An emphasis is placed on detailing the flame-heater modeling as well as issues that arose during development. This chapter is concluded with a validation section including the changes that were necessary to reasonably match the model predicted results with experimentally measured data.

Chapter 4 describes the results that were gathered using the validated numerical model. Discussed first are gas temperatures results which play a crucial role in determining diesel engine startability. Also paramount to engine cold start success, intake gas composition is covered along with flame-heater fuel consumption. Finally, a parametric study which was conducted to optimize heater operation is discussed and the results of this study presented along with additional experimental test data.

The thesis concludes with Chapter 5. Here the general conclusions drawn from the study are presented along with recommendations for continued research.

Chapter 2: PHYSICAL SYSTEM

2.1 ENGINE

The diesel engine studied in this project features a 12 cylinder, 90 degree opposed “V” configuration with 1790 cubic inches of displacement. This engine platform comes in varying outputs, rated between 750 and 1500 gross indicated horsepower depending on the desired configuration. Table 1 summarizes the main characteristics [11].

Table 1: 1790 c.i. diesel engine specifications

Displacement		1790 in.^{3} (29.33 L)
Dry weight		5100 lbs (2313 kg)
Horsepower at rated RPM (gross)		750-1500 hp (560 – 1120 kW)
Rated engine speed	Governed (full load)	2400 rpm
	Governed (no load)	2650 rpm
Cylinders		12, 90° V
Bore		5.75 in. (146.05 mm)
Stroke		5.75 in. (146.05 mm)
Camshaft		Dual-overhead
Air system		Turbocharged, after-cooled
Fuel		JP-8, DF-A, DF-1, DF-2

The engine is air-cooled via large fans mounted between the two cylinder banks. This eliminates the failure points associated with liquid cooling systems and helps maintain a small footprint. Also of interest are the engine's abilities to be run completely submerged, and most important for this study, to reliably start at temperatures as low as -25°F.

2.2 FLAME HEATER

To assist the auto-ignition process at sub-zero ambient temperatures, a flame heater located between the turbocharger compressor outlet and the intercooler inlet provides heat to the incoming intake air. This flame heater generates heat by combustion of the same fuel used to power the engine, in the case of this investigation, JP-8. The heater consists of three primary components: a fuel injector, an igniter, and housing. When activated, the fuel injector sprays a fine mist of fuel directly upstream of a spark plug which serves to ignite the stream of fuel. The resulting combustion generates a large flame in the intake path releasing a considerable amount of heat to the combustion gases and unburnt air. This (now warmed) mixture of air, fuel and combustion products is inducted into the cylinders, where additional fuel is injected. JP-8 combustion can be modeled with the following (global) chemical equation (excluding minor products of combustion).

$$C_{11}H_{21} + 16.25\,(O_2 + 3.773\,N_2) \Longrightarrow 11\,CO_2 + 10.5\,H_2O + 61.31\,N_2 \qquad (2)$$

This exothermic reaction releases approximately 6630 kJ of energy based on the lower heating value of JP-8. Since the flame-heater is located in the intake air path, the goal of preheating the air must be carefully balanced with the need to supply enough oxygen to sustain combustion in the main chamber. The rate of fuel delivery is the primary means by which flame-heater operation can be controlled. This is accomplished both by careful selection of the nozzle used for fuel injection as well as control of the fuel supply pressure. In practical applications, the nozzle spray pattern and flow rate curve are selected as part of the design process, so to adjust the flame-heater operation post-production, alterations must be made to the fuel supply pressure. This can be accomplished by altering the fuel pump voltage or by pulsing the pump on and off.

2.3 EXPERIMENTAL SETUP

To validate the developed numerical model against the actual system, experimental data was needed. The engine was tested in an environmental chamber capable of operating in the range of 236 Kelvin to ambient temperature. The test chamber was equipped to chill not only the surroundings, but the make-up air as well. During the tests, the chamber temperature was set at 241 Kelvin and maintained to within approximately 2 K of this set point for the duration of the test (defined as the time between start of engine cranking and reaching stable idle).

To gather data, an array of probes and sensors were fitted to the various engine components. The measured data included: exhaust runner temperatures, intake manifold skin temperature, test chamber ambient temperature, fuel tank temperature, turbocharger inlet temperatures, make-up air temperatures, engine oil temperatures, battery and starter voltages, engine speed, as well as flame heater fuel supply pressures. Additionally, the intake system was instrumented with J-type thermocouples (Pyromation model: J28E-00-15-F3B072-4) arranged downstream of the flame-heater. A general layout of the experimental setup and these thermocouple locations are shown in Figure 1. This layout of thermocouples was chosen to capture the spatial temperature gradients present at the flame-heater outlet. This was important to test the assumptions made in section 3.2, and to calculate a spatially averaged gas temperature for comparison with those predicted by the one-dimensional model. Between the center and each outermost thermocouple, experimental results showed a maximum deviation of 277 Kelvin, indicating a highly stratified gas temperature; however, this deviation averaged over the entire run was on the order of 60 K. Thermocouples were also installed farther downstream in each of the intake runners to monitor air temperatures directly entering each cylinder.

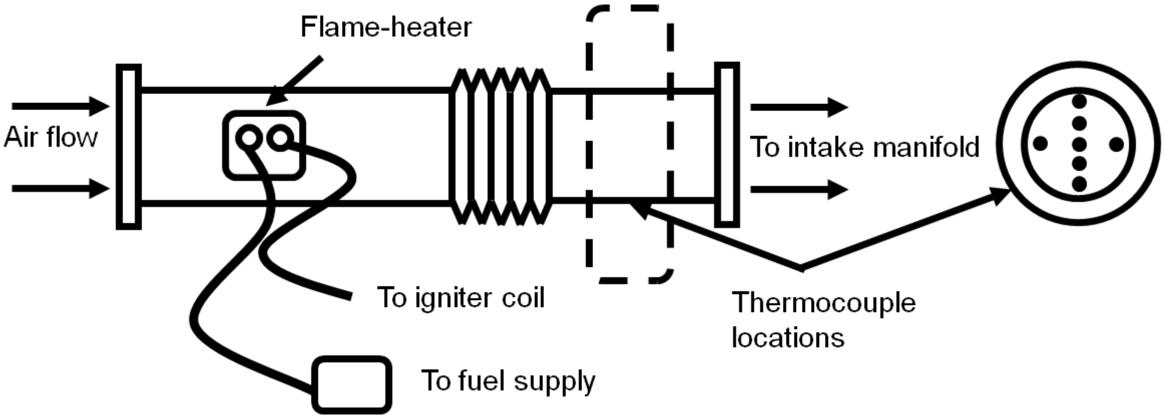

Figure 1: Schematic of flame-heater and thermocouple locations

The data acquisition hardware consisted of a National Instruments (NI) SCXI chassis and thermocouple input modules.

Prior to the test, the engine was allowed to reach thermal equilibrium with the surroundings at 241 K. Cranking runs were conducted with the flame heater activated, while the temperature downstream of the flame heater was simultaneously recorded with 200 Hz sampling rate by the NI instrumentation. Data were recorded for approximately 180 seconds for each run. This testing procedure was repeated for a number of tests with varying results. In most cases, engine cranking speed remained constant to within approximately 10 RPM until initial engine firing. In some cases, engine firing directly lead to engine acceleration and stable idling, while in others, initial combustion events were intermittent and additional cranking time was required to reach a stable idle.

Chapter 3: MODEL DEVELOPMENT

3.1 MODELING SOFTWARE

Gamma Technologies' GT-SUITE was chosen as the primary means to numerically model the selected diesel engine. GT-SUITE consists of a number of separate software modules, each corresponding to different modeling tasks. For the purpose of this study, GT-POWER was used exclusively.

3.1.1 NUMERICAL METHOD

At the core of the GT-POWER code lays a numerical integration strategy for the discretized one-dimensional Navier-Stokes equations. Presented below are the one dimensional formulations for the continuity, energy and momentum equations which are discretized to be solved by numeric integration. Beyond these equations [12], the applicability of the software is expanded by the addition of numerous mathematical models to represent terms such as heat transfer, combustion, phase-change and chemical reaction kinetics.

Continuity: $$\frac{dm}{dt} = \sum_{boundaries} \dot{m} \tag{3}$$

Energy: $$\frac{d(me)}{dt} = -p\frac{dV}{dt} + \sum_{boundaries}(\dot{m}H) - hA_s(T_{fluid} - T_{wall}) \tag{4}$$

Enthalpy: $$\frac{d(\rho HV)}{dt} = \sum_{boundaries}(\dot{m}H) + V\frac{dp}{dt} - hA_s(T_{fluid} - T_{wall}) \tag{5}$$

Momentum: $$\frac{d\dot{m}}{dt} = \frac{dpA + \sum_{boundaries}(\dot{m}u) - 4C_f\frac{\rho u|u|}{2}\frac{dxA}{D} - C_p\left(\frac{1}{2}\rho u|u|\right)A}{dx} \tag{6}$$

where:

$\dot{m}$ boundary mass flux into volume, *dV*

m mass of the volume

V volume

p	pressure
ρ	density
A	flow area (cross-sectional)
A_s	heat transfer surface area
e	total internal energy (internal energy plus kinetic energy) per unit mass
H	total enthalpy
h	heat transfer coefficient
T_{fluid}	fluid temperature
T_{wall}	wall temperature
u	velocity at the boundary
C_f	skin friction coefficient
C_p	pressure loss coefficient
D	equivalent diameter
dx	length of mass element in the flow direction (discretization length)
dp	pressure differential acting across *dx*
dV	volume of discretized element

3.1.2 DISCRETIZATION

To numerically solve these equations, first the modeled system must be broken down into individual sub-volumes, as shown in Figure 2. Discretization of the geometry is defined by the user and requires a balance between solution accuracy and computational expense.

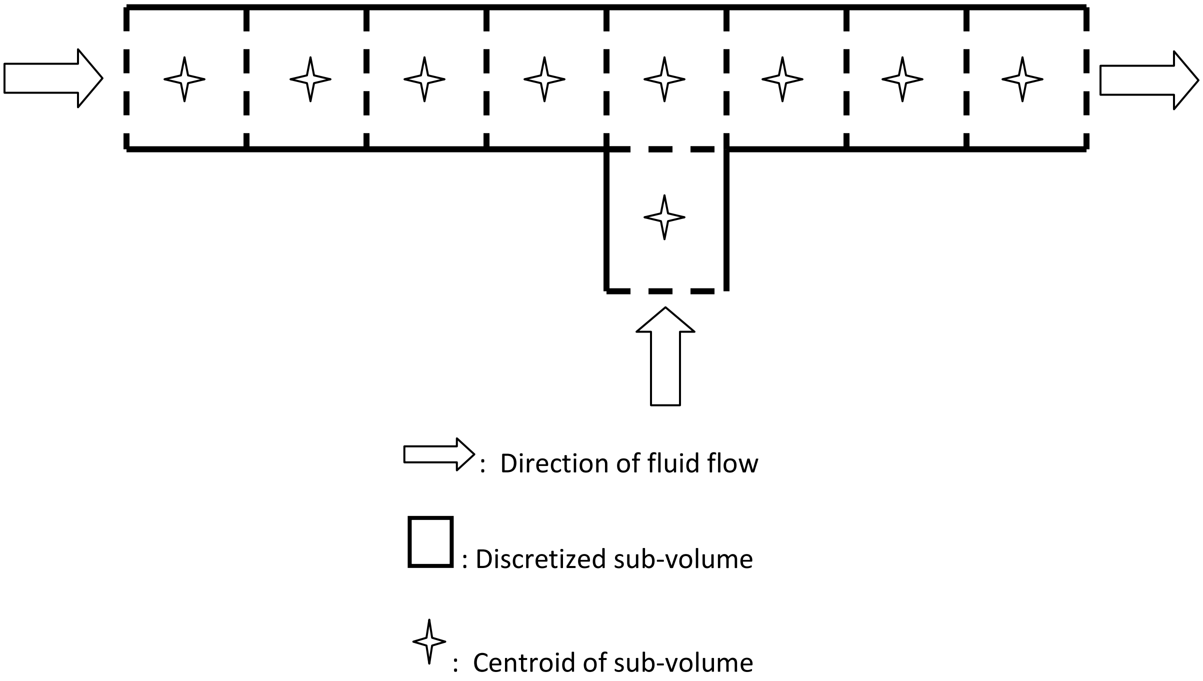

Figure 2: Illustration of 1-dimensional discretization strategy

Pipes and continuous flow components can be discretized into any number of sub-volumes, while components with branching flow, such as splits and collectors, are represented as one discrete sub-volume. By defining the system in this way, calculable quantities must be averaged either over the boundaries of each sub-volume, or over the entire volume. Scalar quantities such as density and temperature are averaged over the entire volume and are taken at the central point of each sub-volume. Vector quantities such as velocity are averaged across each sub-volume boundary.

Numerical solution of the resulting discretized Navier-Stokes equations is accomplished either by an explicit or implicit integration technique. It should be noted that the implicit scheme solves the enthalpy formulation (equation 5), whereas the explicit solves the energy equation. Though the implicit method is typically recommended for longer thermal response studies, this method was precluded by the template chosen to model the flame-heater which required that the explicit solver be employed. While the exact explicit integration scheme built-in to the GT-POWER code remains proprietary, the general operation of this type of solution can be shown with equation 7.

$$\theta(t + \Delta t) = F(\theta(t)) \tag{7}$$

where,

θ	State of the numerical system at any time, *t*
F	Some function or set of functions which relates the state of the system at a current time, to one at a future time
Δt	Some small finite interval of time

In the GT-POWER explicit solver, the function relating the state of the system at a given time to the state of the system in some future time is a relationship between the solution variables of the two adjacent discretized sub-volumes. This is a common approach in many numeric integration schemes such as the MacCormack or Lax-Wendroff methods [13]. While the resulting functions are readily solved, in order to ensure numeric stability, a suitably small timestep must be chosen to satisfy the Courant condition [12] shown below.

$$\frac{\Delta t}{\Delta x}(|u| + c) \leq 0.8 * \lambda \tag{8}$$

where,

Δt	timestep in seconds
Δx	discretization length (m)
U	fluid velocity (ms^{-1})
c	speed of sound (ms^{-1})
λ	user defined multiplier

While this condition helps to ensure the chosen integration scheme is stable, it does not preclude non-physical phenomena from affecting results, as is discussed in section 3.7.

3.1.3 COMPONENT MODELING

Modeling physical components and systems with GT-POWER is accomplished through the use of predefined templates. Select templates are preloaded into each model based on the type of study desired. Additional templates can be added to any model from the template library. To describe a component, the most appropriate template must be chosen and defined with values from the physical system. These include quantities such as geometric constraints, fluid properties or flow rates, heat transfer characteristics, and other material properties. Once a template is adequately defined, it is considered a GT-POWER object and can then be linked to and interact with additional objects to form a complete model.

3.2 ASSUMPTIONS

As with any modeling endeavor, a number of assumptions were necessary to either fill in the gaps where information was missing or unobtainable, or to simplify complex physical phenomena. Listed below are the most relevant assumptions that were made during numerical model development.

- **Air-fuel mixture entering the flame heater can be treated as a pre-mixed homogenous charge.**

  While this is known not to be true, modeling the mixing process in the flame-heater is not supported in the standard GT-POWER code. However, the effects of mixing, namely the fraction of injected fuel actually consumed, were accounted for by careful control of the modeled flame-heater combustion. Information regarding this process can be found in sections 3.6 and 3.7.

- **Three-dimensional effects on combustion and heat transfer processes can be neglected.**

  This assumption was necessary given the one-dimensional nature of the software package used to create the model. To facilitate comparison between simulation predicted results, and those measured experimentally, data gathered from the physical system was spatially averaged removing any dependence on the non-axial directions.

- **Test facility conditions can be modeled as a quiescent chamber at a constant sub-zero temperature.**

  Based upon the experimental data received, this assumption holds until the engine idles for an extended period of time, at which point the chamber temperature starts to increase at the rate of approximately half a Kelvin per second. Since the present simulations focus on the cranking period before engine idle, this assumption is expected to introduce negligible error.

- **Flow pulsations resulting from intake valve operation can be neglected in the regions of the intake system under investigation.**

  This assumption was necessary, since at the time of study, the intake system model was not coupled with an engine model capable of simulating pulsations in the intake runner flow. Neglecting flow pulsations could have a non-negligible effect on the predicted results, particularly the convective heat transfer. Kearney et al. [14] demonstrated the effect of pulsatile flows, as shown in Figure 3.

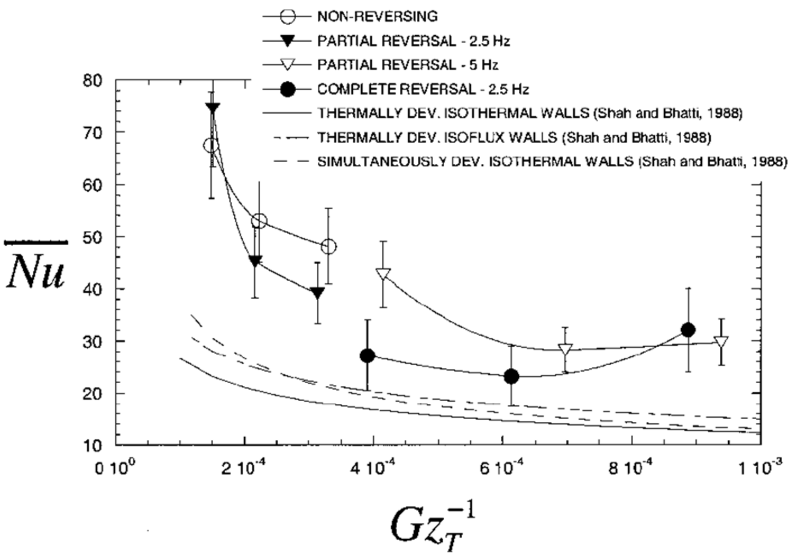

Figure 3: Kearney et al., results of pulsatile flow [14]

From the figure, it is clear that a substantial impact on the Nusselt number can result (depending on the Graetz number) for pulsatile flows when compared with steady flows. This phenomenon could partially explain the discrepancies observed between the predicted intake runner gas temperatures and those measured. These are discussed in sections 3-8 through 3-10. With Womersley numbers ranging between α=15 to α=30 in the regions of interest, the flow would be expected to exhibit a relatively flat velocity profile rather than the traditional parabolic profile associated with more viscous flows, and could significantly alter convective heat transfer when compared with a steady flow. However, with amplitudes of the pulsations being quite small and frequencies on the order of 1 Hz, research conducted by Habib et al. [15] suggest changes to the Nusselt number would not be greater than 5%.

- **Both engine banks behave equally (flow distribution, etc).**

  This assumption was made to simplify the model and reduce overall computational expense. Experimental data revealed relatively small differences on the order of 10%.

This assumption is, therefore, not expected to introduce considerable error, but could be altered by the inclusion of the second bank if further studies were desired.

- **The cylinder head can be treated as a heat sink coupled to each intake runner.** Since the subject of study was primarily the intake system of the engine, flow through the cylinder head was not modeled. To account for any potential heat transfer effects introduced by the cylinder head, it was treated as a lumped mass to which heat from the intake runner flanges could flow. During model testing, very little heat was observed to transfer to the cylinder head via conduction from the intake runners, so this assumption is not anticipated to be a great source of error.

3.3 GEOMETRY

With a log-style manifold and relatively straight pipes, the intake system of the studied engine lent itself well to modeling with GT-POWER. The model geometry for each component (with exception of the flame-heater) was modeled using *PipeRound*, *FlowSplitTRight*, and *EndFlowCap* templates. For reference, Figure 4 has been included showing a representative schematic. All tubular components including the intake elbow, manifold log, and runners were modeled with *PipeRound* templates. Here the length, diameter, bend, material properties, initial conditions, and discretization criteria are specified. At each junction between flow components (i.e. runners branching off main manifold log), a *FlowSplitTRight* was employed. All geometrical constraints, material properties and initial conditions were specified in accordance with available prints and actual test conditions. Pipe wall thicknesses and roughness characteristics were input as part of a *WallTempSolver* template which assists in modeling heat transfer between the working fluid and solid boundaries.

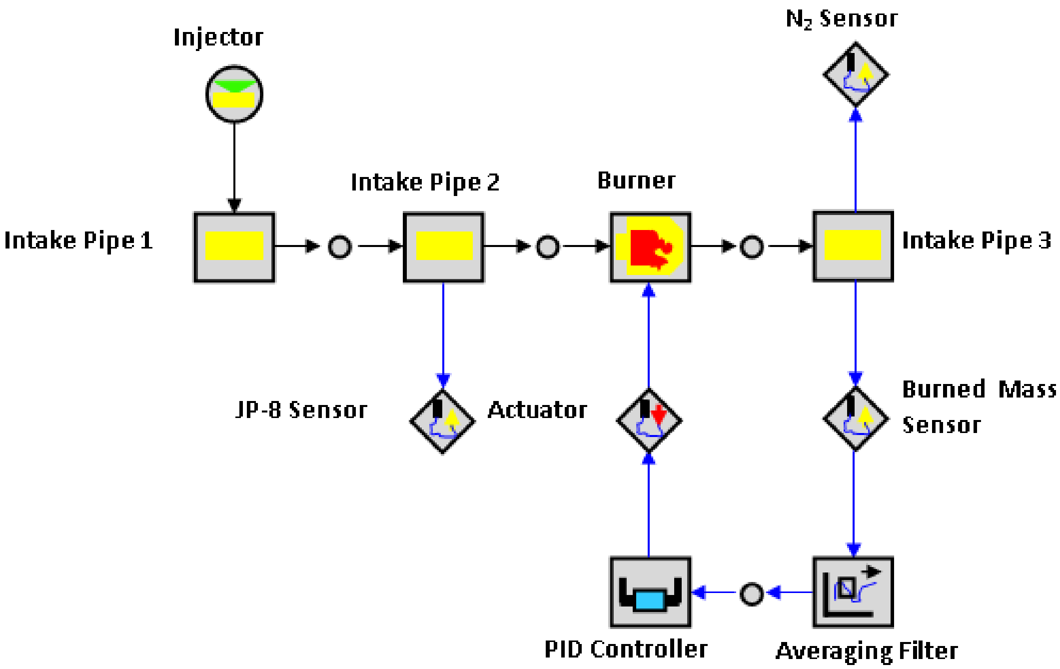

Figure 4: Schematic of flame-heater model with corresponding GT-POWER objects

After defining the flame-heater geometry, it was coupled with a model of the intake manifold to allow exploration of the gas temperatures and composition at the intake ports. The manifold geometry was specified in a similar manner to that of the flame heater using *PipeRound* and *FlowSplitTRight* objects. Figure 5 illustrates the layout of the manifold, although for brevity only half is shown. Since this model was not coupled with a full engine model, each runner exhausts to an outlet defined as containing air at ambient conditions.

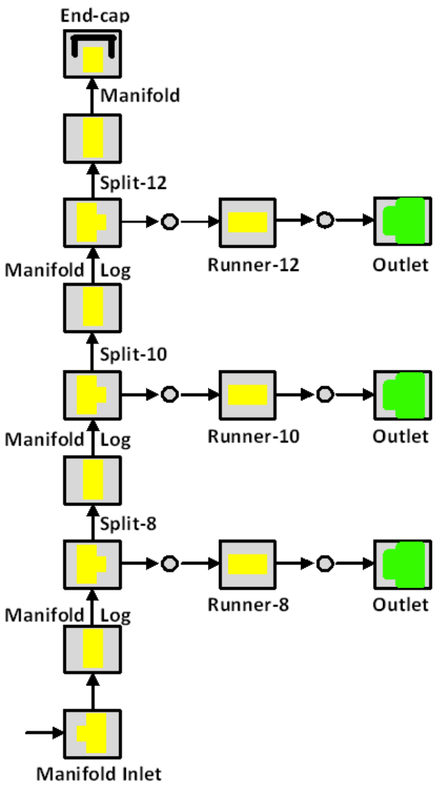

Figure 5: Schematic of intake manifold showing general layout

3.4 MATERIALS

Relatively few materials were needed for creating the intake system model. The following table describes the materials that were employed as well as their respective application.

Table 2: Materials used during intake system modeling

Material Model	Application
jp8-vap* [17]	Vaporized fuel
n2-vap	Air constituent
o2-vap	Air constituent
jp8-combust* [17]	Liquid fuel injected to flame-heater
Air	Primary working fluid
CarbonSteel	All intake components
MagnesiumOxide	Shielded j-type thermocouple

*Material properties were not included in standard GT-POWER libraries and were later defined from additional sources

3.5 JP-8

While a number of common fuels are included as part of the GT-POWER standard library, the fuel of interest for this study, JP-8, was only included as a non-combustible model. Therefore, to simulate the combustion of JP-8 in the flame-heater, a properly defined fuel object had to be created. JP-8 is a kerosene-based fuel, different from Jet-A (aviation fuel) by the addition of icing and corrosion inhibitors, as well as antistatic improvers [16]. Due to its ability to fuel anything from supersonic aircraft to generators, JP-8 has been the fuel of choice for the U.S. military's single fuel initiative. The *jp8-combust* fluid object[1] was defined from the non-combustible *jp8* object in the GT-POWER *FluidLiqCompress* library and modified to more closely approximate the properties of the fuel used in the experiments. The parameters defined for the *jp8-combust* fluid object and corresponding values are displayed in Tables 3, 4 and 5[17, 18]. The coefficients listed in Table 4 characterize the specific heat as a function of temperature following the relationship in equation 9, where T is the operating temperature and T_{ref} is defined as 298 K. Other properties (e.g., viscosity) were specified as temperature-dependent arrays according to [17].

$$C_p = a_1 + 2a_2(T - T_{ref}) + 3a_3(T - T_{ref})^2 \tag{9}$$

Table 3: Relevant properties of aviation fuel JP-8

Parameter	***JP-8 Combust*** **Object Value**
Density @ 298 K (kgm^{-3})	805
Heat of vaporization @298 K (kJkg^{-1})	335
Curve fitting coefficient a1	1972
Curve fitting coefficient a2	2.1875
Curve fitting coefficient a3	0.0

---

[1] This object uses the vapor transport properties of JP-4

Table 3 - Continued

Parameter	***JP-8 Combust* Object Value**
Average chemical formula	$C_{11}H_{21}$
Average molecular weight ($kgkmol^{-1}$)	153.3
Lower heating value ($kJkg^{-1}$)	43,240
Critical temperature (K)	681.1
Critical pressure (bar)	23.4

Table 4: Chemical and thermodynamic properties of JP-8

Property	jp8-vap	Property	jp8-combust
Molecular Weight	153	Vapor Fluid Object	jp8-vap
Carbon Atoms	11	Heat of Vaporization @ 298K	333,500 J/kg
Hydrogen Atoms	21	Density	805 kg/m^3
Oxygen Atoms	N/A	Absolute Entropy @ 298K	N/A
Nitrogen Atoms	N/A	Enthalpy Coeff. a1	1972
LHV	43240 kJ/kg	Enthalpy Coeff. a2	2.1875
Critical Temperature	770 degF	Enthalpy Coeff. a3	0
Critical Pressure	340 psi		
Absolute Entropy @ 298K	Ign		
Enthalpy Coeff. a1	1700		
Enthalpy Coeff. a2	1.45		
Enthalpy Coeff. a3	0		
Enthalpy Coeff. a4	0		
Enthalpy Coeff. a5	0		

Table 5: Transport properties of JP-8

Temperature (C)	Dynamic Viscosity (kg/m-s)	Thermal Conductivity (W/m-K)
jp8-combust		
-20.15	.003602345	.1223
-10.15	.002656642	.1205
-0.15	.002056877	.1188
9.85	.001590029	.117
19.85	.001333432	.1152
29.85	.001097328	.1135
39.85	9.28842E-4	.1117
49.85	8.1048E-4	.11
59.85	7.01949E-4	.1082
69.85	6.18463E-4	.1064
79.85	5.364E-4	.1047
89.85	4.86116E-4	.1029
99.85	4.36677E-4	.1012
109.85	3.73142E-4	.0994
119.85	3.55073E-4	.0976
129.85	3.22625E-4	.0959
139.85	2.97987E-4	.0941
jp8-vap		
303.15	8.02E-06	.00829904
373.55	6.75E-06	.00829904
435.35	8.48E-06	.00829904

3.6 FLAME HEATER MODELING

Initially, to model the flame-heater in GT-POWER, two potential options were considered: the *Burner* template and the *Global Reactions* template. In both models, which are available as part of the GT-POWER after-treatment library, it is assumed that a premixed charge enters the flame heater. Though it was expected (and later experimentally verified) that a highly stratified condition exists in practice, this simplification had to be made since modeling the mixing process was not a capability of the native GT-POWER code given its one-dimensional nature.

The *Global Reactions* template, which allows the user to specify any type of chemical reaction desired using the appropriate chemical kinetics, is primarily used to simulate exhaust catalyst effects. This option was particularly desirable due to the flexibility of the template, and the potential for more careful study of the chemical processes involved in the modeled combustion. However, the lack of information to validate the chemical kinetics of JP-8 fuel compounded with difficulties in simulating the onset of combustion precluded its use. Efforts therefore, focused on using the *Burner* template to model the flame-heater.

The *Burner* template is a simulation tool that works similarly to any other flow component except that any combustible fuel passing through is burned, and the resulting heat of combustion is transferred to the working fluid. The amount of fuel available for combustion (and hence the heat release) can be controlled through adjustment of a parameter known as the time constant *TC*, according to equation 10. Here X_f is the burned fuel fraction and *dt* is the simulation time step (in seconds). It is also important to point out here that the burned mass (see equation 11) refers to both the fuel and air consumed during the combustion process.

$$X_f = \frac{dt}{10^{-6} TC + dt} \qquad (10)$$

$$X_f = \frac{\dot{m}_b}{\dot{m}_t} \qquad (11)$$

where,

$\dot{m}_b$	Total burned mass flow rate through burner template
$\dot{m}_t$	Total mass flow rate through burner template

The time constant is, in essence, a calibration parameter which was used to calibrate the model against experimental test data. This process is described in section 3.8. Internally, the model uses the burned fuel fraction to determine how much fuel should be combined with the available oxygen and calculates the products of combustion using equilibrium chemistry and the resultant heat release.

The average residence time of the mixture in the burner is given by the ratio of the burner length and the mixture velocity. At each time step, the amount of combusted fuel results in the burned fuel fraction given by equation 12. This implies that a larger-than-specified amount of fuel will be burned when the residence time of the mixture in the reactor is greater than one time step. Assuming, for instance, that the user specifies a *TC* value that leads to $X_f = 0.9$ (see equation 12); if the residence time is such that the mixture remains in the burner for three time steps, then the total burned fuel fraction will be:

$$X_{f\ TOTAL} = \underbrace{0.9}_{\text{Time step 1}} + \underbrace{(0.1)(0.9)}_{\text{Time step 2}} + \underbrace{(0.01)(0.9)}_{\text{Time step 3}} = 0.999 \qquad (12)$$

That is, at each time step, the “base” burned fuel fraction (0.9) multiplies the fraction of unburned fuel that remains in the burner from the previous time step. This dependence on both the velocity of the air-fuel mixture (hence on the engine cranking speed) and the simulation timestep made controlling the amount of fuel consumed and the resulting heat release extremely difficult and unpredictable. An alternate control strategy, further discussed in section 3.7, was devised to overcome this difficulty.

3.7 MODEL INSTABILITY

With the geometry, material properties and combustion model created, early simulations were run to evaluate the model's performance. Initial testing of the intake system model revealed considerable non-physical instability for any burned fuel fraction lower than unity. In order to isolate the conditions (or main contributors) to the observed instabilities, a number of simulation cases were run with varied burner lengths, time constants, and inlet velocities. General simulation conditions are summarized in Table 6. The test cases were selected after observing relationships between model instability and both burner length and fluid velocities. To fully investigate these relationships a very broad range of test conditions was established. Though each condition does not necessarily represent an actual operating point or reasonable geometry, the extreme values were selected to evaluate model sensitivity to a particular parameter (e.g. length). Another important factor to control for was the simulation time step. Although the time step is automatically determined by the code to improve simulation efficiency, constant time steps can be specified if the step size assigned by the user is less than that calculated by the software. Since, according to equation 10, the time step affects the residence time and corresponding fuel fraction burned, it was set at a constant value of 10^{-6} to exclude its effect in the study. A selection of specific test cases is shown in Table 6, and corresponding results can be seen in Figures 6a through 6h.

Table 6: General test conditions employed during stability study

Parameters	Range of values considered	Phi	Time step
Burner length	0.01-8000 mm	~0.7	1E-6 sec.
Inlet velocities	0.1-15 m/s	~0.7	1E-6 sec.
Time constant	0-5000	~0.7	1E-6 sec.

Table 7: Selected cases from stability study chosen to highlight results

Case	Velocity (m/s)	Time constant	Length (mm)
A	0.1	0	50
B	0.1	500	50
C	8.0	50	50
D	15.0	50	50
E	20.0	50	50
F	0.1	50	5
G	0.1	50	500
H	0.1	50	5000

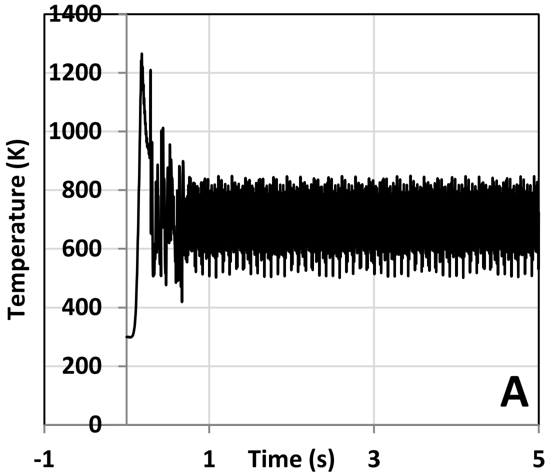

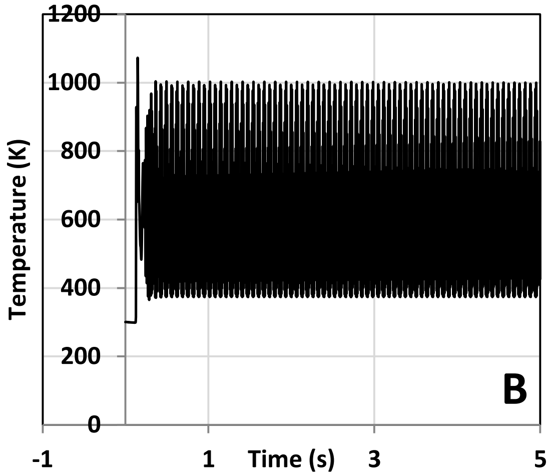

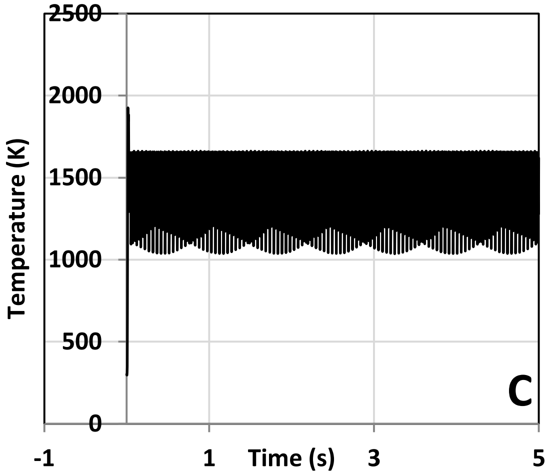

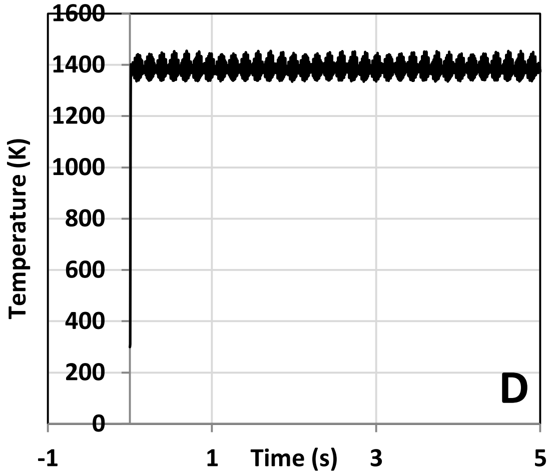

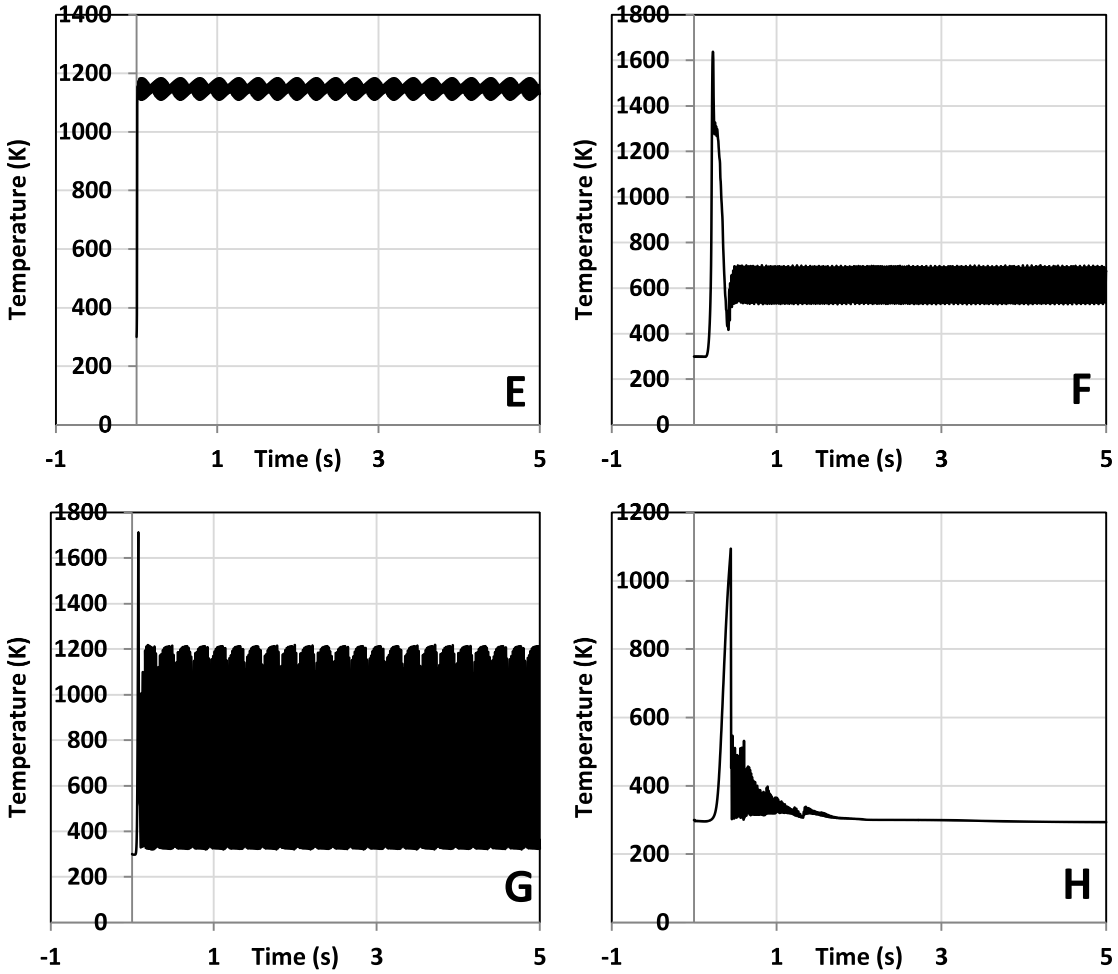

Figures 6a-6h: Instantaneous flame-heater gas temperatures from stability study

In cases *a* and *b*, the time constant was increased from 0 to 500, while maintaining the length and inlet velocity constant. Referring to equation 10, increasing the time constant (TC) results in a lower fraction of fuel burned. Although a constant X_f value may be expected because both the time step and *TC* remain constant, there will be some variability in the residence time (due to the changing velocity), which affects X_f. Comparing figures 6a and 6b, it can be seen that greater instabilities arose with increasing value of time constant (i.e., lower amounts of burned fuel). In cases *c*, *d*, and *e*, the velocity was increased while the time constant and burner lengths remained constant. The instabilities can be seen to decrease as the mixture velocity at the burner inlet increases. In cases *f*, *g* and *h*, the burner length was progressively increased while the remaining two parameters were maintained constant; the instability in the results first increase, and then decrease at lengths greater than one meter. These instabilities in the simulation results were ultimately attributed to fluctuations in the mass flow rate of air through the flame-heater and were closely linked to heater operation through the sub-volume density calculation. Figure 7 illustrates how dramatic these fluctuations were. Since the exact numeric integration strategy used by the GT-POWER code has not been released, only speculations can be made as to the exact numeric explanation for the problem. It is thought, however, that the treatment of the heat released from combustion in the *Burner* template, which would be traditionally handled as a source term in the energy equation, impacts the calculation of the average density. The density then influences the mass flow rate through the *Burner* which in turn disrupts steady combustion. This interplay between the heat release due to combustion and the mass flow rate is thought to be the root cause of the instability.

To remedy the problem and better regulate flame-heater operation, a simulated proportional-integral-derivative (PID) control loop was developed to fix the percent fuel burned to a desired value throughout the simulation. The control loop works as follows: a target value for the percent fuel burned, $X_{f,}$ is specified in the case setup as a constant or time-dependent array. The actual percent fuel burned is calculated by monitoring the mass fraction of JP-8 entering and exiting the flame-heater. This calculated quantity is then used as the input to the PID controller. The PID controller adjusts the time constant value to match the actual percent fuel burned to the desired value. With this method, the instability of the results can be controlled. In addition, the model can be more readily calibrated, since the percent fuel burned is a more physically intuitive parameter than the time constant.

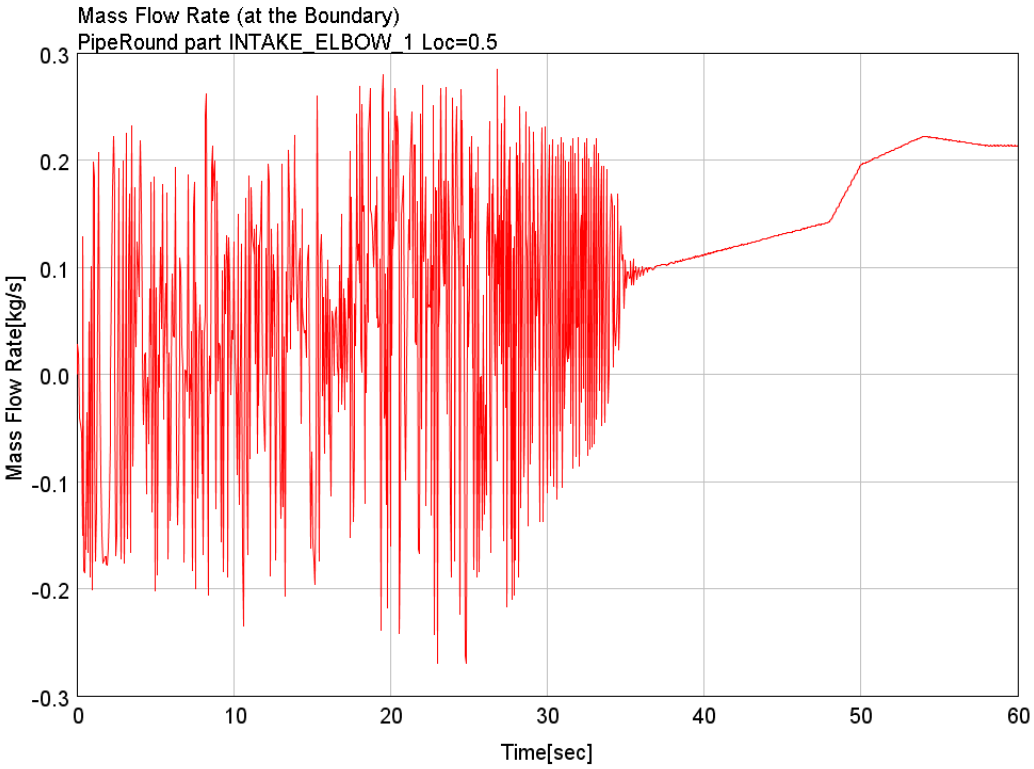

Figure 7: Predicted mass flow rate through flame-heater without PID control loop

The implemented control loop consists of a burned mass fraction sensor, averaging filter, controller, and actuator. To calibrate the controller for optimal response, gains were first calculated using a proprietary spreadsheet supplied by Gamma Technologies. These values were then further refined through a process of trial and error to provide rapid response while minimizing overshoot. The results of this addition dramatically reduced the instabilities witnessed in previous testing (shown in Figure 7) while enabling more precise control of the fuel fraction burned; however, certain cases still produced instability in the mass flow rate of the working fluid, as seen in Figure 8.

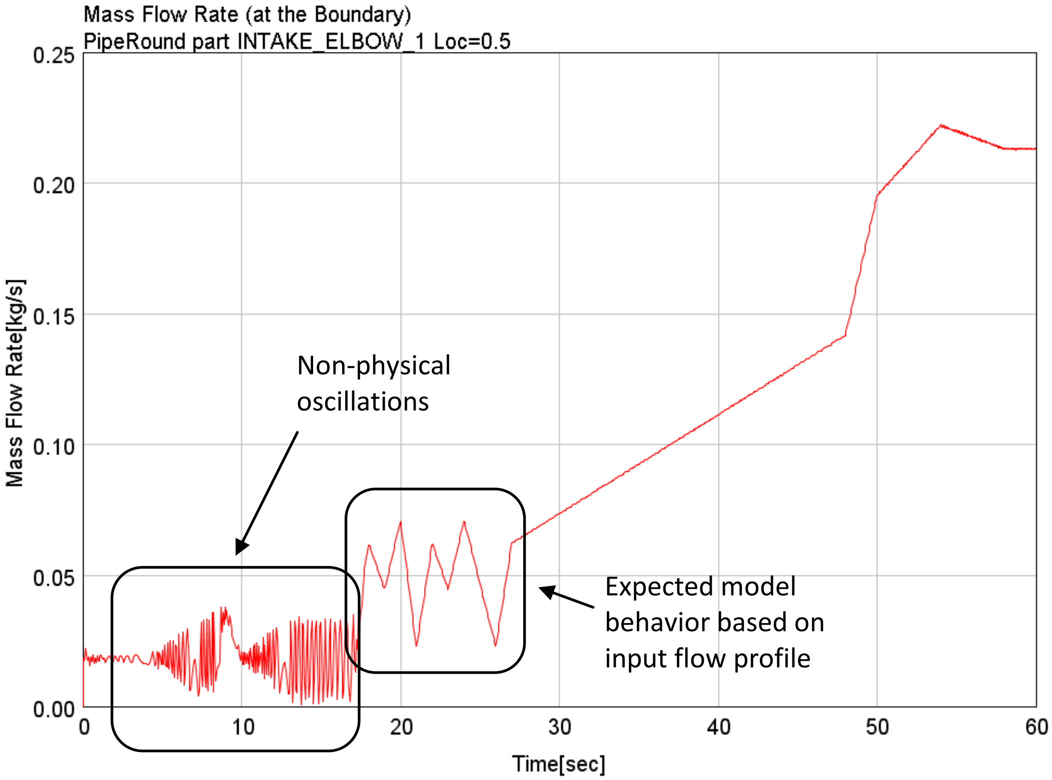

Figure 8: Predicted mass flow rate through flame-heater with addition of PID control loop

Here it is evident that while the PID loop helps mitigate any instability for higher mass flow rates, in the low mass flow rate regime, non-physical instability still manifests. Ultimately, eliminating these fluctuations required redefining the inlet boundary. The inlet boundary was originally defined as a volumetric flow rate, but was changed to a mass flow rate definition. By doing so, any dependence on the fluid density was removed, and all previous instabilities were eliminated, as shown in Figure 9. For clarity, the peaks at the 10 second mark, as well as the oscillations around the 20 second mark, were actual inputs to the model introduced to match rapid engine speed changes in the experimental test run.

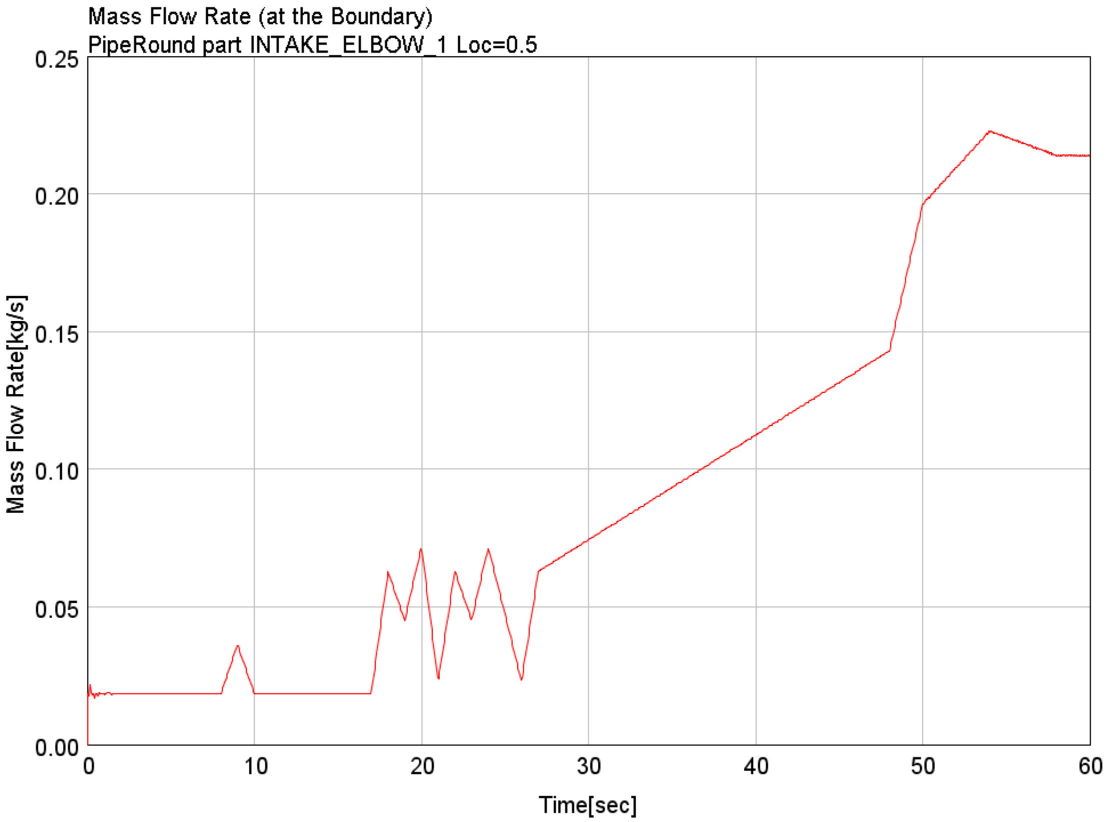

Figure 9: Predicted mass flow rate through flame-heater with PID loop and redefined intake flow profile

3.8 FLAME-HEATER VALIDATION

Validation is one of the most important steps in performing any computational fluid dynamics (CFD) analysis. Incorporating the flame-heater, the temperature directly downstream of the heater was chosen as the target variable to validate the GT-POWER intake system model. This selection was made based on a number of criteria; first, temperature measurements are readily obtained from the experimental setup and require minimal modifications for installation. Second, since gas temperature is one of the most influential factors in the calculation of chemical species concentrations, it plays a crucial role in determining the properties leading to successful cold start. Finally, whenever possible it is desirable to isolate system variables under investigation, so by measuring gas temperatures directly downstream of the flame-heater, heat transfer effects can be minimized allowing the flame-heater model to be effectively decoupled from the heat transfer model. This is important since inaccuracies in the heat transfer model will affect the predicted flame-heater gas temperatures and would distort any attempts at calibrating its operation.

The main drawback to validation using experimentally measured temperatures downstream of the flame-heater is the suspected non-uniform temperature distribution at the heater outlet. Since GT-POWER models this in one spatial dimension, stratification of the heat release in the non-flow directed axes cannot be captured in the model. To account for this, an array of seven thermocouples was installed to measure the temperature at multiple spatial points, as shown in Figure 10; this test procedure is outlined in section 2.3. These values were averaged and compared to the model-predicted temperature at the same downstream location.

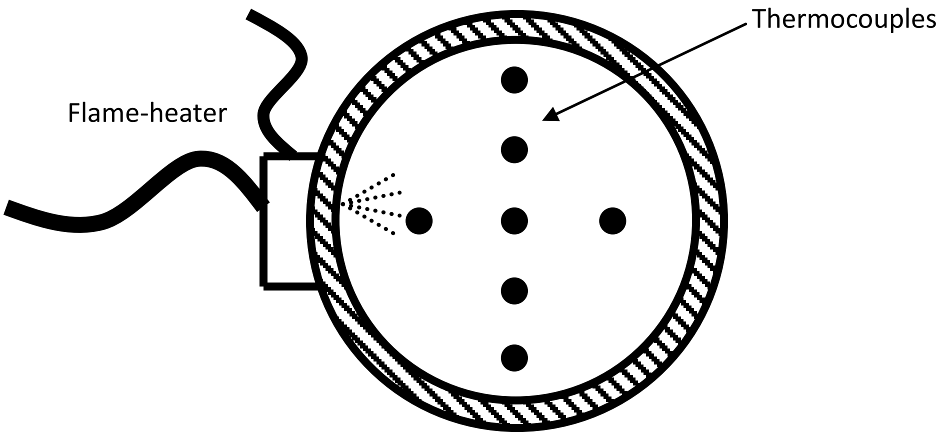

Figure 10: Schematic of thermocouple location in relation to flame-heater orientation

Experimental data used to validate the flame-heater revealed that the engine operated at constant speed for approximately 30 seconds before accelerating to stable idling. Initially, the model was run using a constant intake air mass flow rate to match the mass flow rate calculated from the constant engine cranking speed. During these attempts, significant disagreement was found between the model-predicted and experimental temperatures downstream of the flame-heater after the initial cranking period (Figure 11). This disagreement was attributed to two factors. First, the increased flow rate of chilled air had a significant cooling effect on the system. Second, because the intake air flow rate increases with engine speed and the amount of fuel injected in the flame heater remains constant, the mixture became progressively more fuel-lean as the engine accelerated to stable idling. To account for this, a flow rate profile matching that of the test case was implemented. It should be noted here that a constant burned fuel fraction was specified in the flame-heater combustion model (see section 3.6 for details). The burned fuel fraction value was chosen to generate the heat necessary to bring the flame-heater outlet temperatures up to the level observed during testing.

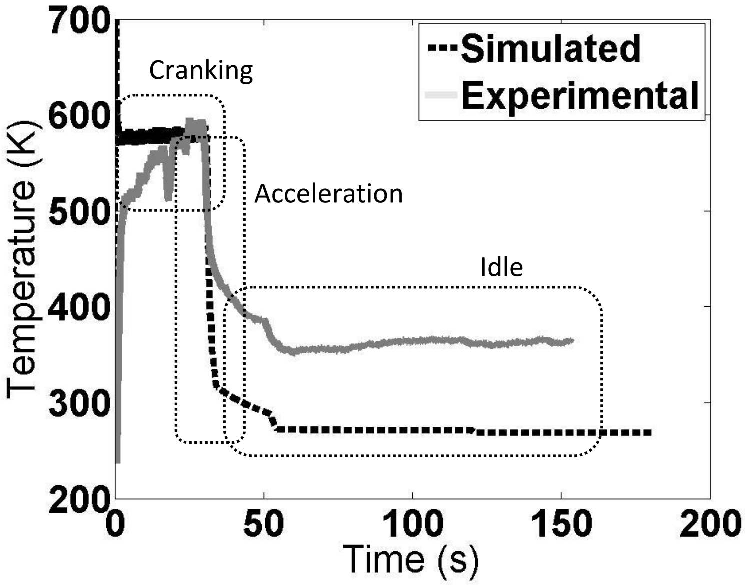

Figure 11: Predicted flame-heater outlet gas temperatures compared with experimentally measured values for initial test. Simulated results presented before the addition of a thermocouple object.

Results are shown in Figure 11. While the experimentally measured and model-predicted temperatures after the initial constant flow rate period (engine cranking) show reasonable agreement, the gas temperatures after engine acceleration and into idle are grossly underestimated. It was hypothesized that with the increased air flow rate of the more rapidly rotating engine, a greater fraction of the fuel may be consumed due to more vigorous mixing and fuel atomization. This would lead to greater heat release in the flame-heater, thus explaining the observed under-prediction of gas temperatures. Since the mixing effects in the flame-heater were not modeled in detail due to limitations in the chosen modeling suite, and no known correlation between air mass flow rate and burned fuel fraction for diesel flame-heaters was available, a linear relationship was assumed. After a number of attempts, the following equation was developed describing the fuel fraction burned as a function of volumetric flow rate. This relationship was determined through a trial and error approach. First, the total burned fuel fraction required to match the experimentally measured gas temperatures was found for the engine speed at idle. With the burned fuel fraction already determined for the engine cranking speed, a linear equation was established. Finally, this equation was slightly adjusted to provide the closest agreement across the entire tested range of engine speeds.

$$X_f = 0.00490928 * \dot{V} + 0.2000 \tag{17}$$

where,

X_f	Burned fuel fraction
$\dot{V}$	Volumetric flow rate (L/s)

This relationship much more accurately captured the gas temperature trends observed in the experimental data, reducing the error during engine idle from roughly 100 Kelvin to approximately 25 K.

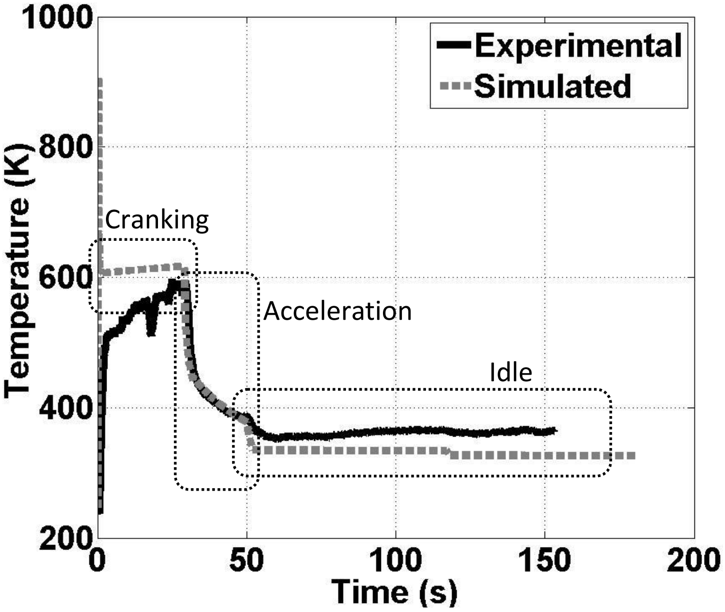

Figure 12: Predicted flame-heater outlet gas temperatures compared with experimentally measured values after implementation of equation 17. Simulated results presented before the addition of a thermocouple object.

With the experimentally measured and model-predicted gas temperatures at the flame-heater outlet closely matching, investigations into the gas temperatures and stoichiometry at the intake runners followed.

3.9 HEAT TRANSFER DISAGREEMENT

After validating the gas temperatures at the flame-heater outlet, analysis of the intake runner gas temperatures was conducted since these more closely impact diesel auto-ignition. Simulation cases were run using a mass flow rate profile matching that of the experimental test cases and the relationship from equation 17 defining flame-heater operation. Gas temperatures in the intake runners were targeted, and results showed disagreement of nearly 150 Kelvin in the worst case when compared to intake runner gas temperatures measured during physical testing. Figure 13 provides an example of this discrepancy. To accurately gauge the effect of changes to flame-heater operation on cold-start success, intake air temperatures at each runner, along with gas compositions are crucial, so before any studies could be conducted related to engine cold start performance, the disagreement between the model predicted and experimentally measured intake runner gas temperatures had to be addressed.

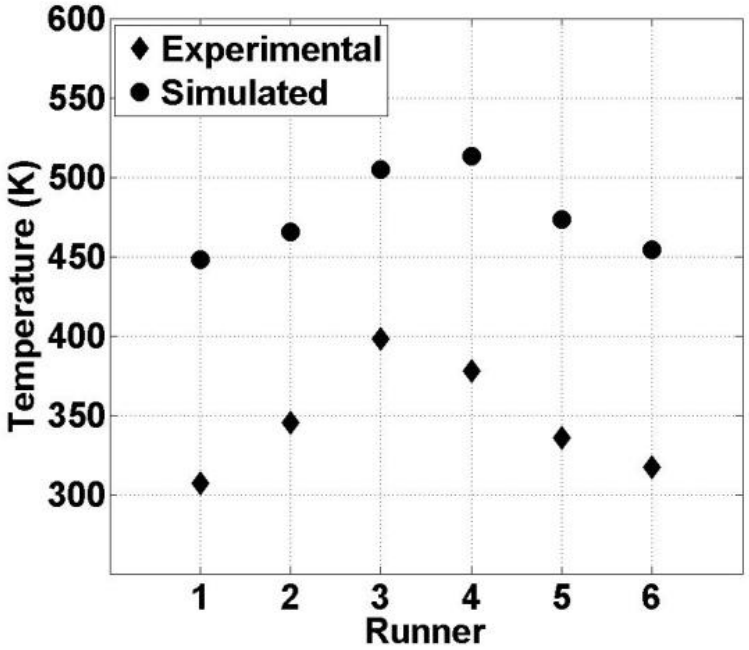

Figure 13: Intake runner gas temperature comparison between model predicted and experimentally measured results

Since the flame-heater combustion (and resulting heat release) had been validated, investigations into the intake runner temperature discrepancy focused on heat transfer modeling. Figure 13 clearly illustrates the dramatic over-prediction of gas temperatures at the intake runners and suggests that the heat transfer from the warmed air leaving the flame-heater outlet to the surrounding intake system was underestimated. To root out the cause of this, both heat losses via conduction and heat loss from convection were examined.

GT-Power provides a number of methods for adjusting and refining heat transfer characteristics of an engine model. One of the main controls is the *WallSolver* object, which can be defined for any flow object. The *WallSolver* object defines all the relevant material properties (e.g., specific heat, thermal conductance, thermal mass, etc.) which may affect the transfer of heat between the flowing fluid and the wall of the flow component (i.e., the intake runner in this case), or the heat transfer between the wall of the flow component and the surrounding ambient air. In addition to this, thermal masses can be added to certain flow components adding conduction losses, and heat transfer multipliers can be employed to scale the convective heat transfer, either globally (for the entire model) or for individual flow components (e.g., individual runners). To correct the observed discrepancy between the model predicted runner temperatures, and those measured, all these methods were investigated.

First, to confirm the validity of the experimentally measured temperatures by accounting for potential thermocouple error, a thermocouple object was created to match those used during testing (Pyromation model: J28E-004-00-15-F3B072-4) of the flame-heater gas temperatures. Being insulated shielded thermocouples, the thermocouple temperature cannot be assumed to directly match the surrounding gas temperatures. The implemented thermocouple object accounts for this thermal response; however, it was shown to have a negligible impact on predicted peak temperatures, varying the results by only 2-3 Kelvin.

Next, conduction losses to the cylinder head which were not originally included in the model were thought to contribute to the variation found between the model predicted and experimental gas temperatures. To remedy this, thermal masses were added to the intake manifold simulating conduction heat losses through the cylinder head. This was accomplished by creating and connecting *ThermalMass* objects to each runner via a runner flange. The *ThermalMass* template is used in GT-POWER to represent a lumped mass to or from which heat can be transferred. Each object defined represented an equal portion of the total cylinder head mass, and was modeled to match the heat transfer characteristics of cast iron. When connected to a pipe, such as the case with the intake runner flanges, the entire convective area is used in the heat transfer calculation unless otherwise specified. In testing for conduction losses, this was desirable to maximize the amount of heat transferred from the working fluid. After applying the mass of the cylinder head to the intake runners, a total of 21.3kg, less than a one Kelvin change was observed in the intake runner gas temperatures. Further, the *ThermalMass* objects' temperatures, shown in Figure 14, did not rise considerably, suggesting negligible heat transfer between the gas and the mass of the cylinder head.

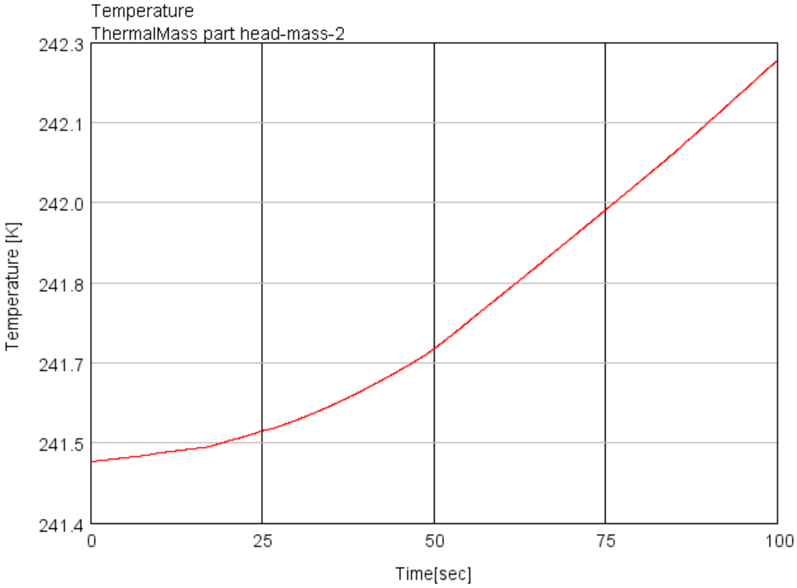

Figure 14: Temperature response of *ThermalMass* object connected to intake runner 2

With conduction losses ruled out and thermocouple errors accounted for, further efforts explored potential errors in the modeling of convective heat transfer. Since the exact surface roughness was not known, the surface roughness of the intake manifold flow components was tested at values between .01mm and 2mm (sand roughness scale) in an attempt to increase the convective heat transfer coefficient by adjusting a parameter with more physical meaning. This process too, however, was shown to have little effect on the intake manifold gas temperatures, as only a 10 Kelvin change was observed across the entire range of tested values. The negligible dependence of the gas flow in the intake runners on surface roughness was attributed to the fact that the flow is in a state of transition-to-turbulence.

After adjusting the parameters with potential physical implications (however negligible the effect), both the global and local heat transfer multipliers were explored. The global heat transfer multiplier, which allows the heat transfer for every flow component to be scaled by a constant value, considerably altered the intake runner gas temperatures. However, it also affected the rest of the model, including the flame-heater. It was found that the calibration of the intake runner gas temperatures could not be decoupled from the downstream flame heater gas temperatures. The local heat transfer multiplier, in contrast, also allows the convective heat transfer to be scaled, but on an individual component basis. Adjustment of this parameter was performed in a two step process. First, a single multiplier value was set for the entire manifold until the predicted temperatures more closely matched the experimental. Then, the individual runner multipliers were further refined until the temperatures matched to within very small margins. While this was a successful strategy, it was not based on anything physical. Also, the heat transfer multipliers had to be adjusted to account for different flow conditions (i.e. changing engine RPM), which yielded the model unusable in practical simulations. These limitations combined with the need for a physical explanation of the discrepancy prompted an investigation into the GT-POWER heat transfer model.

3.10 HEAT TRANSFER MODEL ALTERATION

GT-Power uses the Colburn analogy to calculate convective heat transfer coefficient [12]. For the laminar regime, a constant Nusselt number is employed, and for turbulent flows:

$$h = \left(\frac{1}{2}\right) C_f \rho U_{eff} C_p Pr^{\left(-\frac{2}{3}\right)} \qquad (13)$$

In the transition regime, the convective heat transfer coefficient is linearly interpolated between the turbulent and laminar values. While the Colburn analogy has been studied and used for decades, it is only strictly applicable to cases of fully developed (hydrodynamically and thermally) turbulent flows [19]. Since the intake system of the studied engine consists of relatively short pipes which do not satisfy the conditions for fully developed turbulent flow, the

Colburn analogy may not accurately represent the convective heat transfer (see Table 8 for x/D values).

An alternative correlation (see equation 14), developed based on experimental data and applicable to non-fully developed flows was found better suited to the thermal and flow conditions encountered in the studied intake system. This correlation, presented by Molki and Sparrow [20], was only tested at Reynolds numbers between 9000 and 30,000. Although these values exceed Reynolds numbers in the intake manifold and runners (between 1875 and 4700), this correlation was selected for implementation since it was found to provide the most accurate gas temperatures. It should be noted that correlations developed by Al-Arabi [21] and Hausen [22] were also tested. The Hausen correlation proved similar to the default model, while results from the Al-Arabi correlation were similar to those from the Molki-Sparrow, however slightly less accurate. Results of each correlation are presented in Figure 15.

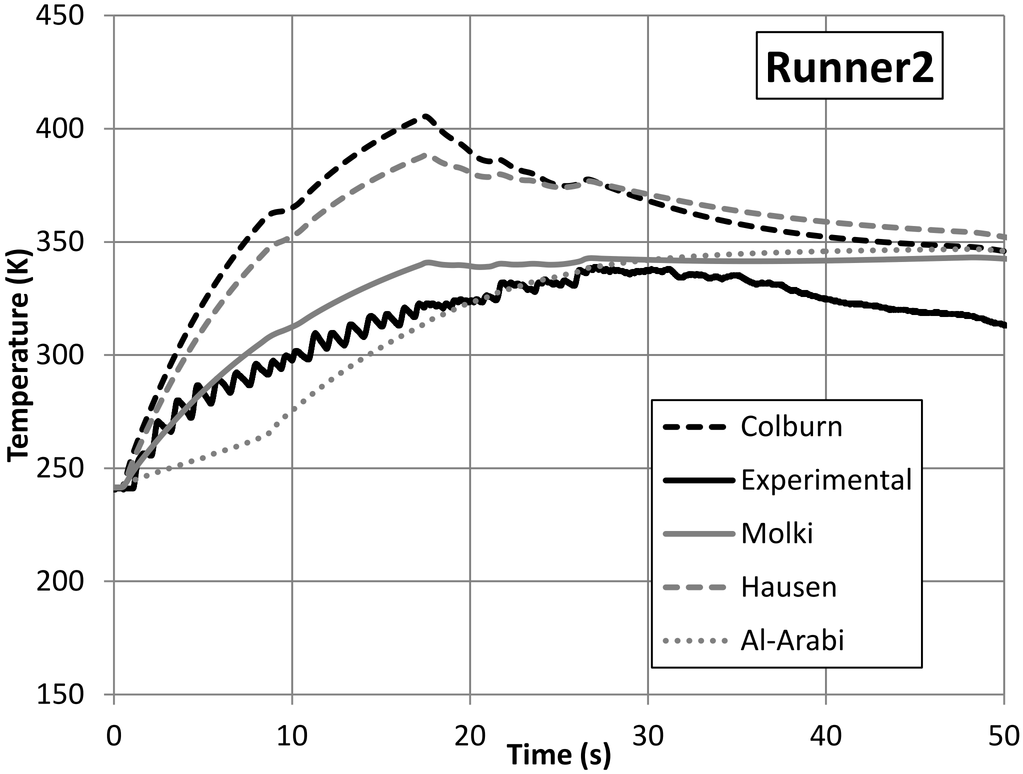

Figure 15: Runner 2 gas temperature results comparison.

$$\frac{Nu_{avg}}{Nu_{fd}} = 1 + (\frac{a}{x/D})^{b} \tag{14}$$

where:

$$a = 23.99Re^{-0.23} \tag{15}$$

$$b = -2.08 * 10^{-6}Re + 0.815 \tag{16}$$

Nu_{avg}	corrected Nusselt number
Nu_{fd}	fully developed Nusselt number
X	distance from the flow inlet
D	diameter of the pipe

Implementing this heat transfer correlation required a correction be made to the Nusselt number calculated by the native GT-POWER code. This correction was applied via a heat transfer multiplier through a number of steps. First, the x/D values for each intake manifold component were calculated. For the main "log" of the manifold, x was taken as the distance from the centerline of the main inlet flow-split to the longitudinal center of the manifold component of interest. For convenience, a schematic of the model has been provided in Figure 16.

Table 8: Updated heat transfer correlation with necessary x/D values

Flow Component	x/D
manifold-body_1	0.76
manifold-body_2	0.76
manifold-body_3-1,3-2	2.76
manifold-body_3-3,3-4	5.25
runners	2.38

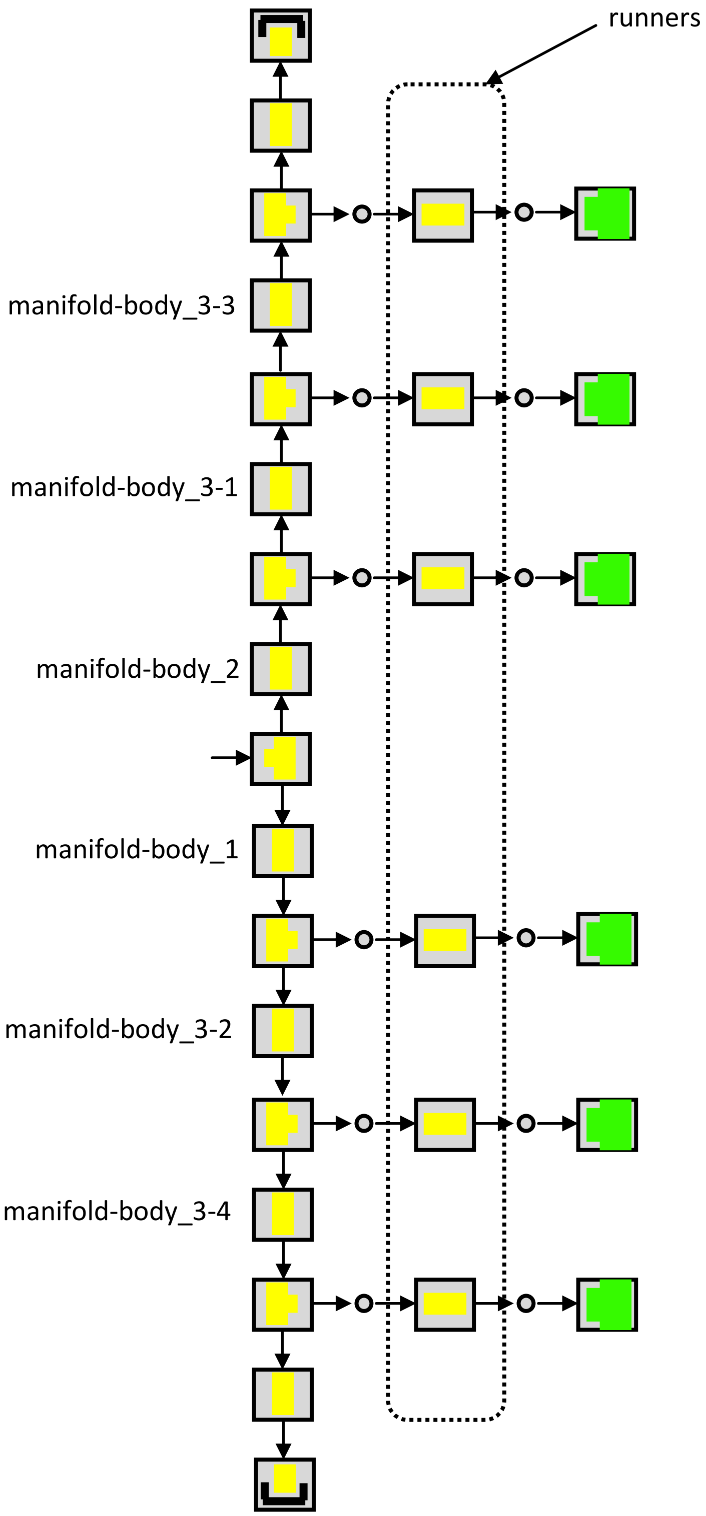

Figure 16: Schematic of intake manifold with labeled flow components corresponding to Table 8

The Reynolds number was monitored throughout the entire simulation and used as an input to a *MathEquation* object. The *MathEquation* object computes the new heat transfer multiplier based on equation 14, and sets the value on a continuous basis. Due to relative similarity in the x/D values and Reynolds numbers between complementary manifold components (i.e. runners 2 and 4, 1 and 6) one *MathEquation* object was used for each pair of manifold components. The following table describes the implementation.

Table 9: Implementation of Nusselt number correction

MathEquation Object	Reynolds number source	Objects applied to
1	manifold-body_1	manifold-body_1, manifold-body_2, mainsplit, runner_split-1, runner_split-2
2	manifold-body_3-1	manifold-body_3-1, manfiold-body_3-2, runner_split-3, runner_split-4
3	manifold-body_3-3	manifold-body_3-3, manifold-body_3-4, runner_split-5, runner_split-6
4	runner-4	runner-4, runner-3
5	runner-2	runner-2, runner-5
6	runner-1	runner-1, runner-6

Figure 17 illustrates the improvements made to the intake runner gas temperature predictions. Here, a case was run for 50 seconds using the same experimental intake flow profile. It is judicious here to mention that both sets of predicted results (default and improved heat transfer models) were generated using the thermocouple model described in the previous setion. The figure indicates much closer agreement between model-predicted and experimental data using the improved heat transfer model (employing equation 14) than had previously been achieved by allowing the code to employ the default heat transfer model (based on the Colburn analaogy) in the calculations. Results predicted using the default model show an overprediction of gas temperatures on the order of 25%, while those predicted with the improved heat transfer model are near 10%. Further, these predictions are based on a physical model, rather than on arbitrarily imposed heat transfer multipliers.

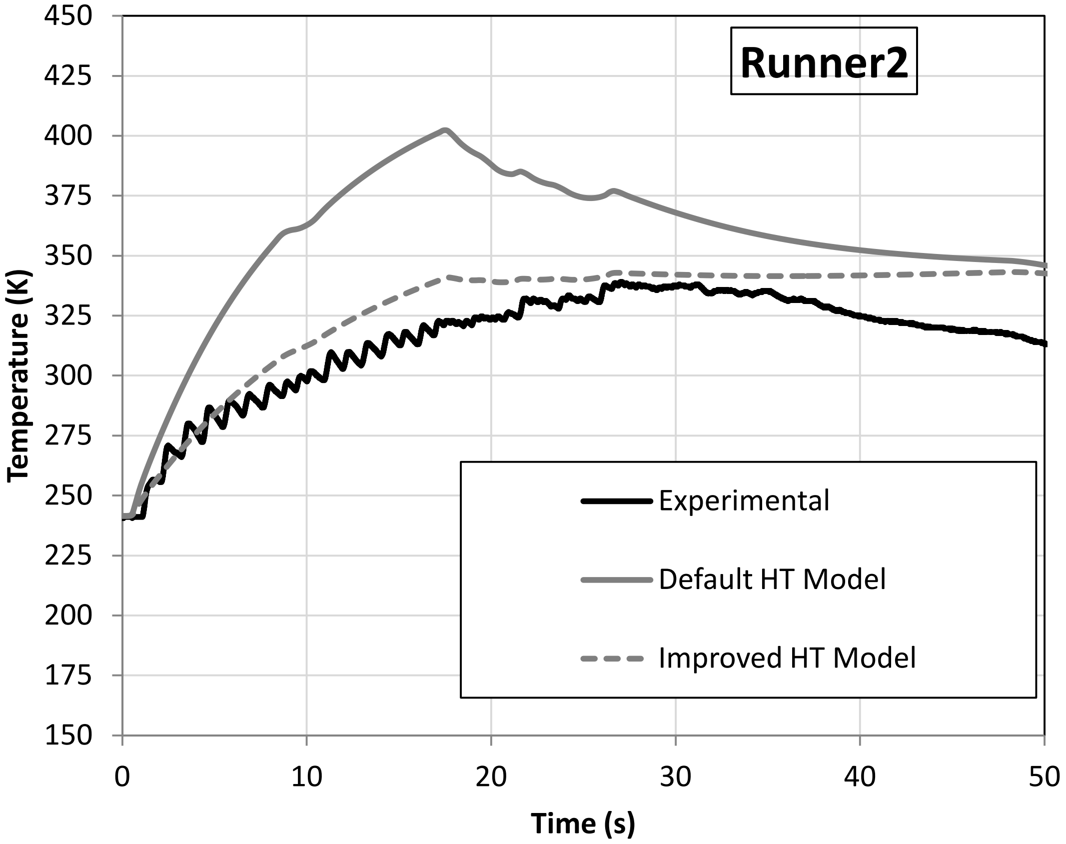

Figure 17: Comparison between default and improved heat transfer models in relation to experimentally measured intake runner 2 gas temperatures

Chapter 4: RESULTS

4.1 TEMPERATURE RESULTS

As discussed in section 3.8, predicted intake runner gas temperatures were over-predicted by as much as 150 Kelvin when compared with experimental data. This led to an in-depth examination of the built-in heat transfer model which was modified from using the standard Colburn analogy for convective heat transfer to using the correlation presented by Molki and Sparrow. With the improved heat transfer correlation in place and the burned fuel fraction validated by comparison with experimentally measured flame-heater outlet data, temperatures at the intake runners were again analyzed. Presented in Figure 18, are comparisons between the experimentally measured intake runner gas temperatures, those predicted with the standard GT-POWER heat transfer model, and those predicted employing the improved heat transfer model based upon the Molki-Sparrow correlation for non-fully developed flows. Overall, the agreement improved over the entire cranking period. The closest agreement was found in runners two and three, with runner four clearly exhibiting the least favorable agreement. These results are summarized in Table 10.

Table 10: Average and peak error of predicted intake runner gas temperatures with improved heat transfer model

	Average Error (50 sec.)	Peak Error
Runner 1	21.46 K	34.54 K
Runner 2	12.49 K	17.99 K
Runner 3	6.78 K	4.13 K
Runner 4	26.64 K	41.98 K
Runner 5	25.83 K	36.81 K
Runner 6	24.48 K	28.62 K

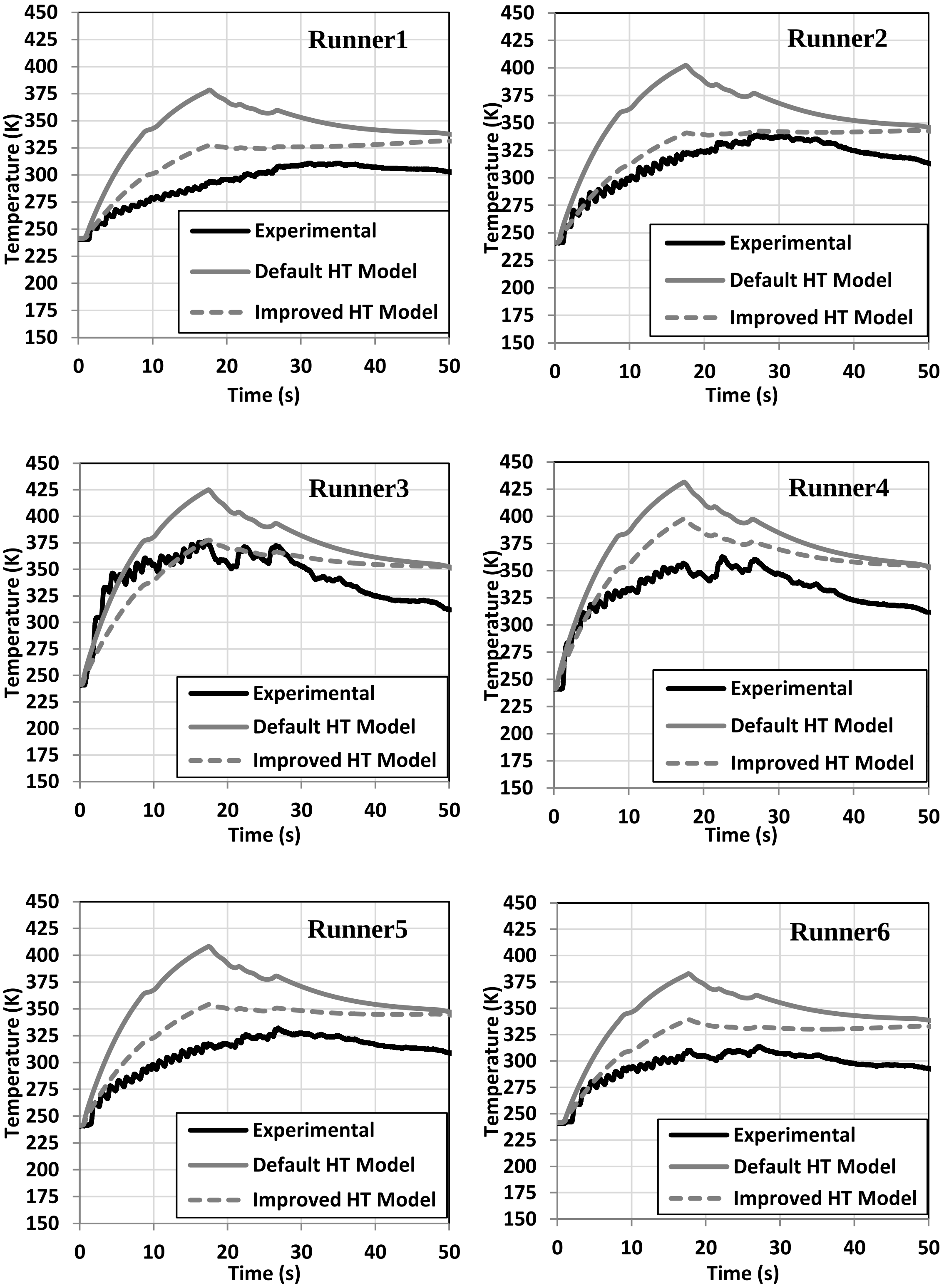

Figure 18: Comparison of predicted and experimental intake runner gas temperatures

Figure 19 displays the overall temperature trends across the manifold. Here gas temperature data was sampled at the point of largest discrepancy between predicted and experimental results (ca. 17 seconds). Also included are error bars describing the potential error in the thermocouple measured temperatures. Overall, the gas temperature trends are well captured, however greater errors are found in one half of the manifold. This phenomenon has been studied with the model, and runner four has been found to have a slightly lower Reynolds number compared with its complementary runner three resulting from slight dissymmetry in the manifold. This reduces the convective heat transfer from the intake charge to the runner wall, thus resulting in a higher predicted gas temperature.

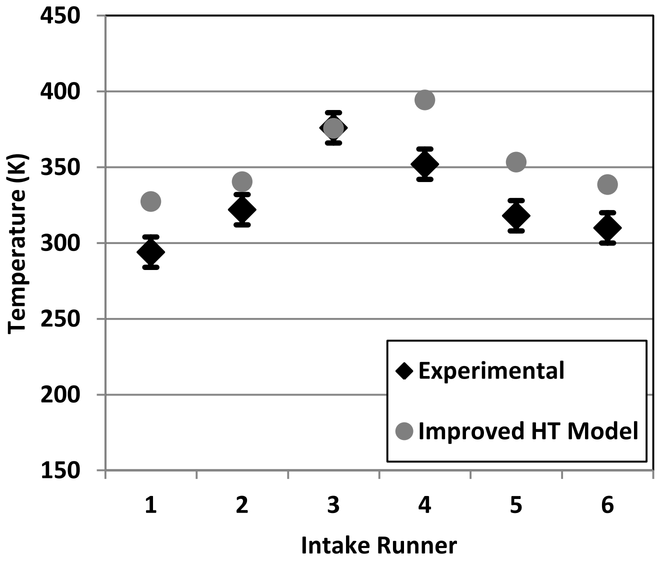

Figure 19: Error analysis of predicted intake gas temperatures with improved heat transfer model

4.2 STOICHIOMETRY

Following validation, an analysis of the predicted gas composition downstream of the flame-heater was completed to examine the concentrations of major and minor combustion product species after the initial (30-second) cranking time. This time period was chosen since it is the most relevant to cold start success. Results from this study are presented in Table 11.

Table 11: Predicted chemical species concentrations at the flame heater outlet

Species	O_2	CO_2	H_2O	N_2	CO	NO	H_2	Total
Mass Fraction	0.0291	0.0367	0.0143	0.2261	1.58E-6	4.17E-4	3.64E-8	**0.307**

As shown in Table 11, the mass fractions of major and minor species sum up to 0.307, which was the burned mass fraction specified as input for the simulation. By adding to this value the mass fractions of unburned vapor and liquid fuel (0.0210 and 0.0052, respectively); and the mass fraction of unburned air (0.6670), a total mass fraction equal to unity is obtained, as expected.

To explore the in-cylinder conditions during cranking for cold-start attempts, an effective equivalence ratio was calculated for each cylinder based upon simulation results for gas composition at the intake runners. While the species concentrations were not directly simulated in the combustion chamber, an indirect method using the intake runner compositions was employed. To obtain the effective equivalence ratio, the gas composition at each runner was first analyzed to determine the mass fractions of unburned fuel (both liquid and vapor), unburned air, oxygen, and nitrogen. Gas composition results at each intake runner for a variety of run conditions are included in Appendix B. It is important to note here that the software defines unburned air separately from remaining oxygen and nitrogen in the products of combustion. For convenience, the remaining oxygen was recombined with appropriate fractions of remaining nitrogen in order to treat the oxygen as reconstituted air. Finally, the predicted unburned fuel was added to the fuel injected into the cylinder to calculate the effective air-fuel ratio at which the engine operates with cold-start assist. Both the liquid and vapor fuel mass fractions were considered in the calculation.

Following this procedure, the effective equivalence ratio for flame heater-assisted starting ranged between 2.0 and 2.6. These values represent the upper limits, since it is unlikely that the full amount of unburned fuel will be transported into the main chamber. However, these were important to determine whether unburned fuel from the flame-heater could affect the equivalence ratio enough to reach the flammability limits of JP-8. As reference, the equivalence ratio for non-assisted starting is 1.7, and flammability limits for JP-8 are shown in Table 12. The volumetric percentages were obtained from [17] and used to calculate the corresponding equivalence ratios, assuming $C_{11}H_{21}$ as the chemical formula for JP-8. These results suggest that during this start-up attempt, flame-heater operation did not hinder engine start ability from a flammability limit standpoint.

Table 12: JP-8 flammability limits

Fuel	**Lean (Lower) Flammability Limit**		**Rich (Upper) Flammability Limit**	
	% by Vol.	**Φ**	**% by Vol.**	**Φ**
JP-8	0.6	0.468	4.7	3.82

The presence of a fuel-fired (flame) heater in the intake manifold increases the charge temperature and alters the mixture composition at the runners. Fundamentally, oxygen is replaced with combustion product species, which is analogous to introducing exhaust gas recirculation (EGR) in conventional applications. The effect of EGR on combustion has been widely documented [23-25]. Söjberg et.al investigated the effect of EGR on combustion phasing in a homogeneous charge compression ignition (HCCI) engine. Three mechanisms were suggested to explain changes in autoignition timing due to EGR addition. First, a (thermodynamic) cooling effect due to a specific heat (C_v) increase of the intake charge by the addition of complete stoichiometric products (CSP); second, a retarding (chemical) effect due to reduced concentrations of O_2 in the intake charge; and third, an enhancing (chemical) effect due to the presence of H_2O in the intake charge [23]. The significance of each was found to be dependent on fuel type. That is, two-stage ignition fuels such as PRF80[2] were found to be more sensitive to a reduction in O_2. The effect was attributed to a reduction in the heat release rate during the low-temperature heat release phase, which reduced the compression temperature and delayed main ignition. Conversely, the presence of water appeared to enhance the early reactions that lead to main ignition. Two-stage ignition fuels were also found to be less sensitive to the cooling effect of EGR.

For the current model, the reduction in O_2 due to EGR addition to the intake charge was estimated using the species mass fractions predicted from the simulation roughly 15 seconds into cranking. This process is described next.

Complete combustion of JP-8 in air is defined by:

$$C_{11}H_{21} + 16.25\,(O_2 + 3.773\,N_2) \Longrightarrow 11\,CO_2 + 10.5\,H_2O + 61.31\,N_2 \qquad (2)$$

Here, air is assumed to consist of 20.95% oxygen and 79.05% nitrogen. The latter figure includes trace gases such CO_2 and argon [1]. Mole fractions of complete stoichiometric products are therefore 13.28%, 12.68%, and 74.04% for CO_2, H_2O, and N_2, respectively. For fuel-lean combustion (i.e., $\Phi \sim 0.7$) of JP-8 and air, without EGR, the ratio of intake charge mass to fuel mass is 20.9. Since EGR is replacing intake air, it is possible to calculate the mole fraction of O_2 needed to maintain a constant intake charge mass-to-fuel mass ratio as the mole fraction of CSP increases [23].

Results are shown in Figure 20. As expected, the mole fractions of CO_2 and H_2O increase linearly as the CSP mole fraction increases. The O_2 mole fraction, on the contrary, decreases, as more of the air is replaced by EGR (in this case represented by CSP).

---

[2] This is a primary reference fuel consisting of 80% isooctane and 20% n-heptane by volume.

Linear fits were generated to quantify the mole fractions of product species (CO_2, H_2O, N_2) as a function of CSP mole fraction, using the data shown in Figure 20. The equations are of the general form:

$$y_i = \pm\ m y_{CSP} + b \tag{18}$$

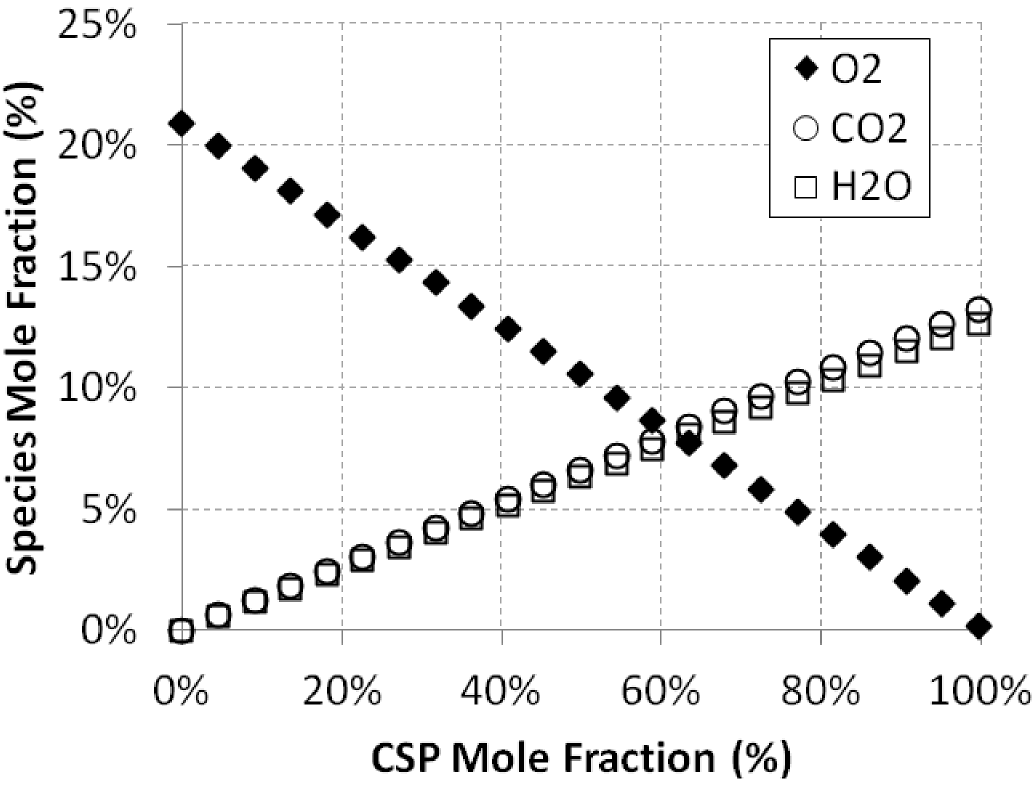

Figure 20: Mole fraction of O2 needed to maintain constant charge mass-to-fuel mass ratio as the CSP mole fraction increases. Fuel: JP-8, Intake charge mass-to-fuel mass ratio =20.8 calculated with air dilution.

The mass fractions of species obtained from the simulations were standardized using equation 19. The values were converted to mole fractions and substituted into the linear fit equations for each species, to calculate the corresponding mole fraction of CSP.

$$mf_i = \frac{X_i}{X_b} = \left(\frac{m_i}{m_T}\right)\left(\frac{m_T}{m_b}\right) \tag{19}$$

This process yielded a CSP mole fraction of 60%. Therefore, assuming that CSP has increased from 0% to 60% (i.e., $\Delta y_{CSP} = 60\%$), O_2 has been reduced by 12.5% (see Figure 20). Note that a 1% reduction in O_2 has been experimentally shown to retard the ten percent burn point (CA10) by approximately 3°CA in PRF80, a two-stage ignition fuel [23], suggesting that O_2 reduction has a non-negligible effect on auto ignition timing. Although excluded in the present analysis, partially oxidized species (e.g., CO and NO) have been found to retard auto ignition in two-stage fuels. Additional studies are needed to further investigate these effects under cold-start conditions.

4.3 FUEL CONSUMPTION

As with the study of virtually any internal combustion engine, fuel consumption was a point of interest while attempting to quantify flame-heater performance. With the fuel delivery rate and gas temperatures at the heater outlet known from experimental testing, calibration of the model consisted primarily of determining the total amount of the injected fuel that was actually consumed. Section 3.8 discusses this process in greater detail, but the conclusion reached was that a large portion of the fuel injected to the flame-heater remained unburned. This value was predicted as high as 69% for low cranking speed cases.

Poor mixing as a result of low mass flow rates of air and poor fuel atomization due to the cold temperatures were thought to contribute to the large fraction of unburned fuel. However, a definitive answer could not be reached without a much more detailed (preferably 3-dimensional) simulation of the injector and mixing processes. To explore this phenomenon and attempt to optimize the heater fuel utilization with the existing 1-dimensional model, a parametric study was conducted in which different fuel delivery profiles were employed.

4.4 PARAMETRIC STUDY

The most readily available method for controlling flame-heater operation is by activation and deactivation of the pump responsible for heater fuel delivery. The nozzle supplying fuel to the unit could also have been modified, but this tack was not desirable due to the effort and expense associated with modifying an existing design. Instead, by pulsing the pump, an average target fuel delivery rate can be achieved based on the frequency and duration of the pulses. With this in mind, a parametric study was conducted to optimize the flame-heater operation by providing the maximum heat release with the lowest fuel consumption.

Since the flow through a nozzle is not linearly proportional to the pressure, and the supply pressure does not act in a purely linear fashion, the dynamics of the flame heater fuel nozzle had to be considered. According to the nozzle specifications [26], a relationship between the fuel supply on/off time and the actual flow rate was established as a piece-wise function.

$$\dot{m}(t_{rising}) = 0.5616t \tag{20}$$

$$\dot{m}(t_{falling}) = -0.0016t^3 + 0.0252t^2 - 0.1754t + 0.7067 \tag{21}$$

where,

$\dot{m}$	Mass flow rate (g/s)
t_{rising}	Time from pump on
$t_{falling}$	Time from pump off

It is prudent to mention here that this fuel flow rate relation assumes that for cases of rising flow, t_{rising} is taken from a point with zero flow, while $t_{falling}$ is measured from a point of peak flow. To implement this relation into the GT-POWER model, a script was written to calculate the appropriate time dependent flow rate profile given a desired duty cycle (i.e., pump-on duration) and frequency. This script was necessary since many of the flow rate profiles tested did not allow ample time to reach either a peak flow or no flow condition. This is demonstrated in Figure 21 . Here, for a duty cycle of 20%, a peak flow condition is not reached on the first pulse; however, due to the slower rate of fuel flow change, the flow does not drop to zero and reaches the peak value on the following pulse.

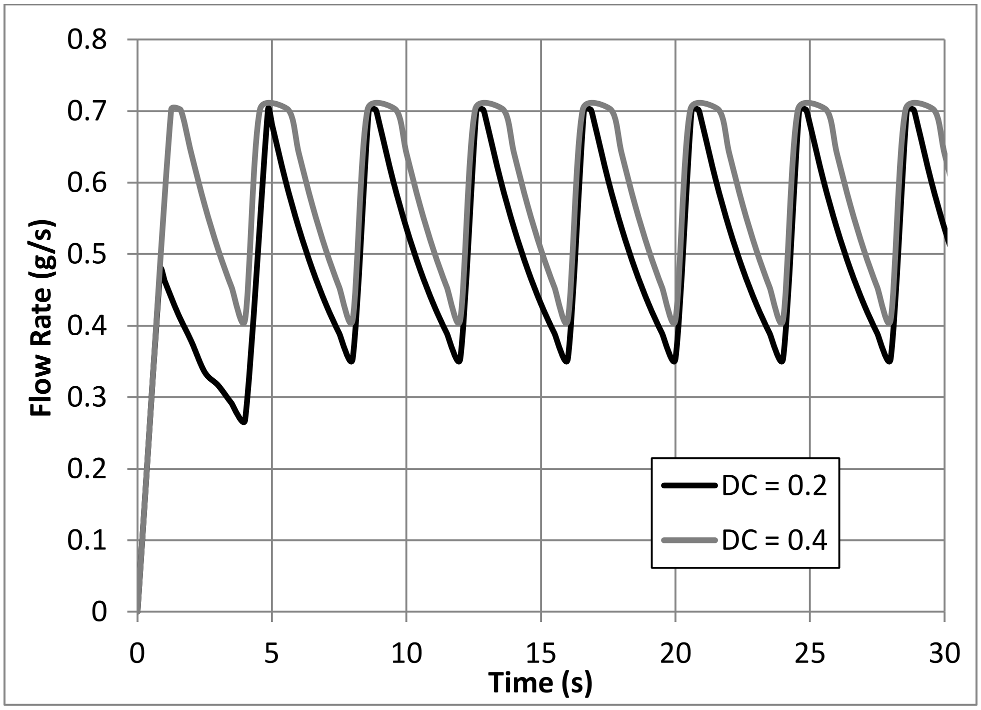

Figure 21: Flame-heater fuel mass flow rate profile for 20% and 40% duty cycles and 5 second period

The fuel supply conditions selected for the study, presented in Appendix A, range from duty cycles of 20% to 80% and pulse period between 4 and 10 seconds. These values were chosen based on two main limitations. First, since the fuel supply switch is controlled manually, there is a physical limit to the frequency of which pulses can be accurately generated. Second, the GT-POWER code requires the fuel supply profile be specified by a series of discrete points which are interpolated between. The resulting data tables are limited in size, so for sufficiently high frequencies, the resolution of the flow rate curve is not fine enough to adequately describe the actual dynamics.

For this study, duty cycles ranging between 20% to 80% were tested along with fuel delivery on-off periods ranging between 4 and 10 seconds. The assessed performance criteria was the maximum flame-heater outlet temperature reached during a 30 second cranking period; 30 seconds being the maximum time generally required for successful cold start attemts. The maximum temperature was optimized with respect to the total fuel delivered to determine an ideal operating configuration. Figure 22 gives a graphical representation of the results of this study.

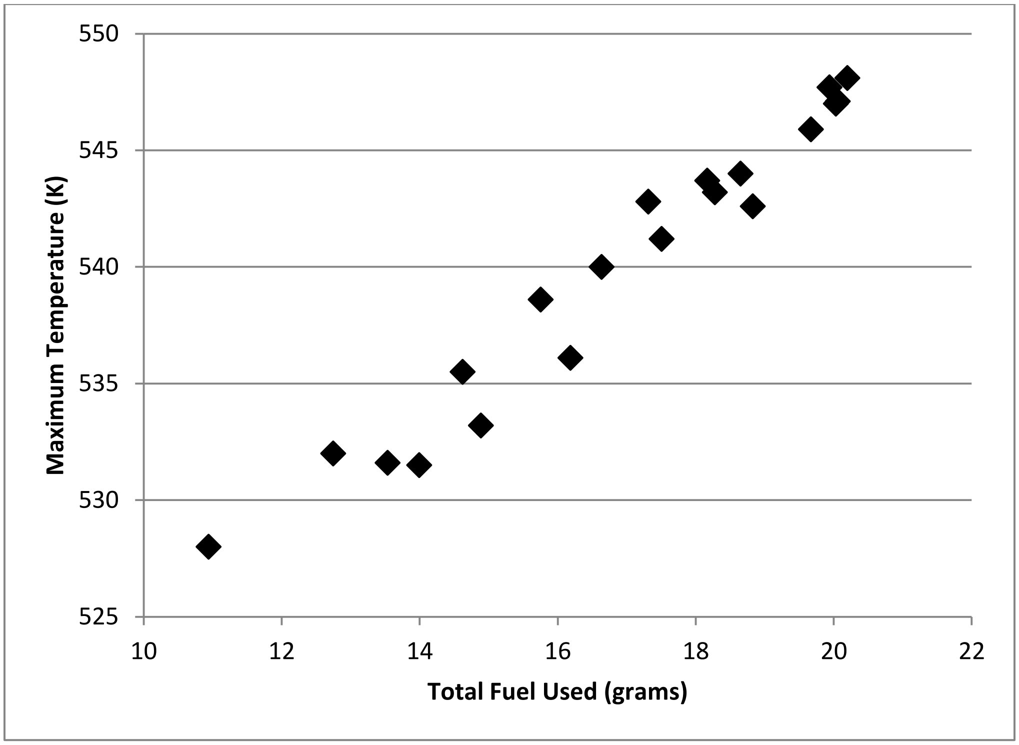

Figure 22: Graphical representation of parametric study results illustrating generally linear temperature trend with respect to total fuel injected

The results demonstrate a reasonably linear relationship between the total fuel used and the maximum temperature reached downstream of the flame heater. There is, however, some amount of variation which illustrated a pattern of optimization potential. For each flame-heater on-off frequency tested, the 20% duty cycle resulted in the greatest maximum temperature for the least total fuel usage. This can be clearly seen in Table 13, which highlights the test matrix employed for the study. Here, the difference between the starting temperature and maximum temperature for each case is divided by the total fuel used and shown as both a function of duty cycle and period.

Table 13: Parametric study optimization matrix

D.C. Period	20%	40%	60%	80%
4 sec.	19.6 K/g	17.4 K/g	16.0 K/g	15.2 K/g
5 sec.	20.7 K/g	17.9 K/g	13.9 K/g	15.2 K/g
6 sec.	21.4 K/g	18.2 K/g	16.5 K/g	15.3 K/g
8 sec.	22.8 K/g	18.9 K/g	16.6 K/g	15.4 K/g
10 sec.	26.2 K/g	20.1 K/g	17.1 K/g	15.5 K/g

It is apparent that smaller duty cycles and longer flame-heater pulse periods result in the greatest maximum temperatures with respect to the total fuel used. Since all other variables were held constant throughout this study (e.g. flame-heater combustion model, air mass flow rate), these variations can only be attributed to fuel delivery dynamics, and may simply be a result of the nature of heat transfer. For cases of higher duty cycles, more total fuel is injected to the heater. This generates higher gas temperatures, resulting in greater heat losses from the fluid to the surroundings. Cases of lower duty cycle then keep a greater percentage of the energy released from combustion in the intake air, but may not necessarily be more desireable. To explore the impact this may have on successful engine cold-start, experimental test data were analyzed to determine if a certain gas temperature threshold could be identified which could reliably predict a successful start. Figure 23 shows the intake runner temperatures for a number of cold start tests. Also included are simulation predicted results for comparison. Here, runners are grouped according to manifold location so that each runner appears next to its complement (see Figures 5 and 16).

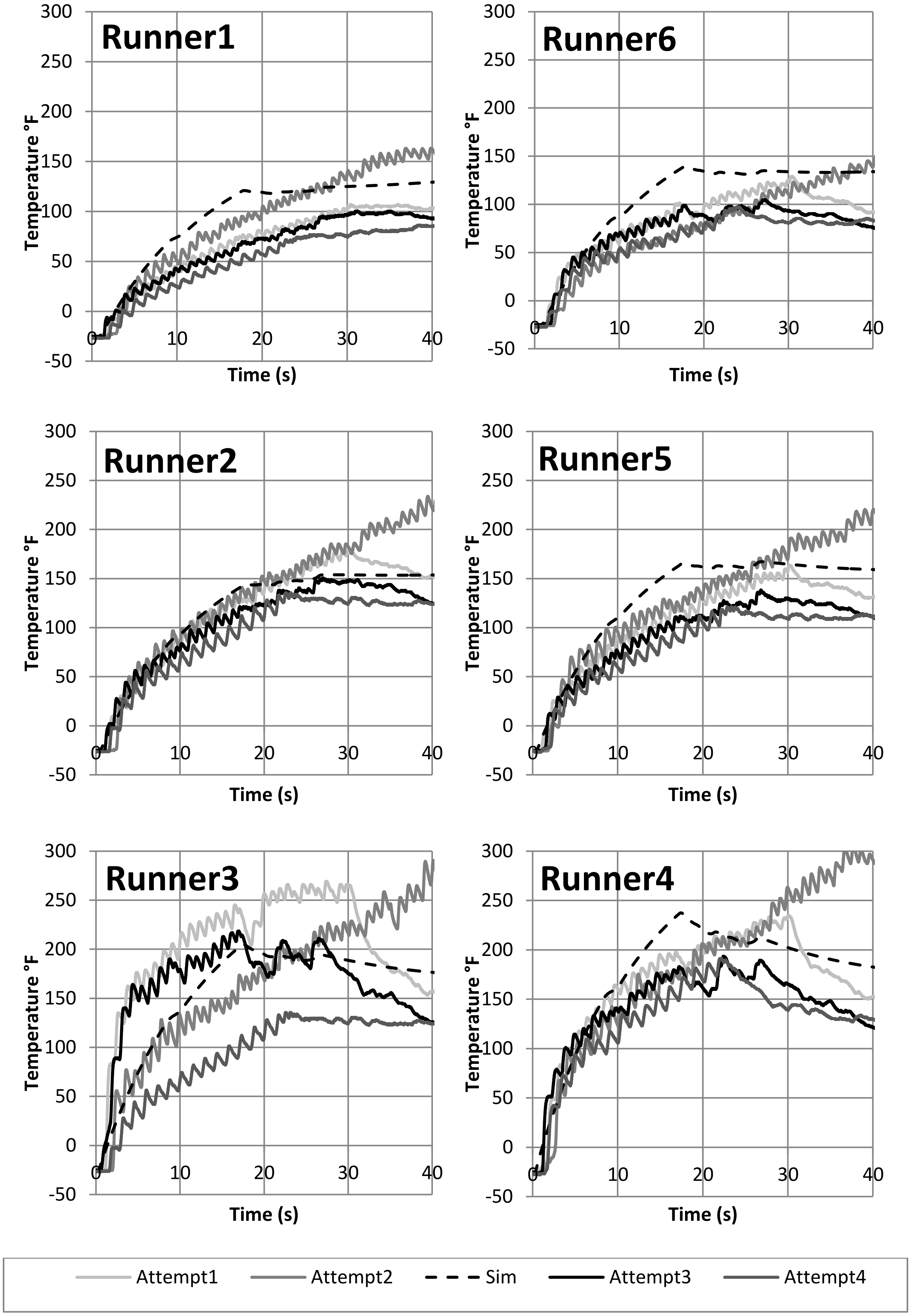

Figure 23: Intake runner gas temperature comparison

Of the experimental test cases presented in Figure 23, all but attempt 2 were successful cold starts. A number of interesting observations can be made from these comparisons. For runner 3, both start attempts 1 and 3 show dramatically warmer gas temperatures early in the run; however, other runners in the manifold do not exhibit nearly as much variability. Interestingly, for runners 1, 2 and 5, the second attempt (the only unsuccessful attempt represented) yields the highest temperatures. Furthermore, these figures do not indicate that a specific intake gas temperature threshold exists as many of the successful attempts (1, 3, and 4) demonstrate temperatures roughly equal to or less than the unsuccessful test. While hypotheses about potential flow differences have been speculated, the phenomena accounting for the dramatically higher runner 3 gas temperatures for the first and third tests remain unknown. Also, with the successful attempt 4 having lower temperatures across the manifold, one would expect the second attempt to have been successful as well. One explanation for this may lie in the difference in average cranking speed between these runs (c.a. 10 RPM) which again points to the delicate relationship between heat transfer and auto-ignition reaction timescales. While a higher cranking speed may generate lower overall intake charge temperatures, the reduction in blow-by losses and increased cylinder pressures might be enough to offset the temperature difference and shorten the ignition delay in accordance with equation 1.

Chapter 5: CONCLUSIONS AND FUTURE WORK

5.1 CONCLUSIONS

So long as diesel engines are employed in power generation, the need to provide consistent reliable operation will remain. Research into the subject of diesel engine cold-start has been ongoing, but for the greater part has excluded flame-heaters as a primary target of study. To help fill a void in the current diesel engine cold-start research and to investigate the conditions conducive to successful cold-start of a real world diesel engine, an intake system model incorporating a flame-heater was developed to simulate cold-start conditions.

In pursuit of the first objective of the work, a model was created with commercial, one-dimensional engine simulation software (Gamma Technologies' GT-POWER). It was generated using all the geometrical constraints and material properties from the corresponding physical system, and in an atypical application, the *Burner template* was chosen to represent the flame-heater. Initial simulation attempts revealed non-physical fluctuations in the intake air mass flow rate, so the model was subsequently adapted with a proportional integral derivative (PID) control loop to enable control over the mass fraction burned and alleviate the observed instabilities.

Following this, the model was calibrated with temperature data gathered from experimental testing. Based on the spatially averaged temperature measurement, simulations predicted approximately 30% fuel mass fraction burned in the flame heater during initial cranking and roughly 70% during subsequent engine acceleration and idle. To account for this, equation 17 was developed, relating the mass fraction burned in the flame-heater with its volumetric flow rate of air.

With the temperatures at the flame-heater outlet validated, additional testing showed that the model correctly predicted gas temperature trends at the intake runners, but exposed a significant discrepancy between the magnitude of the predicted and experimentally measured values. To account for this, an investigation into the built-in heat transfer model revealed that the default heat transfer model was not applicable to the flow being studied. The accuracy of the heat transfer model was improved by implementing a correlation developed specifically for non-fully developed flows. This reduced the error in the gas temperature predictions from over 25% (built-in heat transfer model) to roughly 10% (current model).

And, in achieving the final objective, the effects of the flame-heater on equivalence ratio and mixture dilution were quantified. An effective equivalence ratio was calculated using the predicted product species composition at the intake runners after the first 25 seconds of cranking. With flame heater-assisted starting, the effective equivalence ratio during start-up ranges between 2.0 and 2.6, up to a 53% increase with respect to the reference value. Intake charge dilution was quantified based on substitution of oxygen with complete stoichiometric products (CSP). Based on the predicted mole fractions of product species, the O_2 concentration was reduced by 12.5%, which is equivalent to a 60% CSP increase.

Finally, a parametric study was conducted to optimize flame-heater operation. In this study, the heater fuel supply was pulsed with varying period and duty cycle to maximize the resultant gas temperatures and minimize total fuel burned and thus the overall reduction in oxygen concentrations. Results of this study showed the greatest maximum gas temperatures with respect to total fuel usage were reached with a combination of 20% duty cycle and 10 second flame-heater pulse period. These values, however, may not produce heater gas temperatures high enough to support auto-ignition.

5.2 FUTURE WORK

Supplementary refinement would help reduce model uncertainty and could be done to bring the agreement even closer. Additionally, more studies could be run with the existing or modified model to further research the parameters affecting cold start. The following points highlight some of the recommendations for continuing work.

- **Additional temperature measurements throughout the intake tract, particularly in the intake manifold.**
  Taking additional thermocouple readings at locations between the flame heater and intake runners would allow a much more complete understanding of the heat transfer characteristics of the intake system. This would allow a greater level of refinement of the heat transfer model, and would solidify the understanding of the errors between the model and actual system.
- **An experimental study on the gas composition downstream of the flame-heater.**
  Analyzing the gases exiting the flame heater (e.g., through the use of a tap or potentially an oxygen sensor), would provide additional calibration data beyond only gas temperatures. While the GT-POWER equilibrium chemistry model is thought to be reasonably accurate, without actual gas composition data there is no way of knowing how closely the predicted results match the physical system. Obtaining these results would also help confirm the burned fuel fraction at the flame-heater and further reduce uncertainty in the temperature results.
- **Coupling of the flame-heater model to a complete engine model.**
  To fully understand the cold start problem, it would be pertinent to couple the existing flame-heater model with a full calibrated engine model. While this would require a large amount of data on the studied engine, including all geometrical constraints, air and fuel flow characteristics, and particularly dynamometer results, a fully defined engine model would make conducting cold start studies considerably more revealing. With a fully calibrated model, parameters could easily be varied, and the results would show based on the input conditions whether or not the engine was able to successfully start. This could also help identify any factors which may have been overlooked while

studying primarily the intake system. Of particular interest would be the impact of flow pulsations in the intake system on the convective heat transfer.

- **Perform 3-dimensional CFD analysis of flame-heater, particularly fuel delivery nozzle.** The limitations of the one-dimensional software package chosen to model the intake system prevented a detailed analysis of the flame-heater fuel delivery. The current model predicted a large portion of fuel injected to the heater remained unburned, particularly at low cranking speeds. To understand this process in greater detail, it would be essential to model the fuel delivery and resulting mixing processes in a three-dimensional CFD model. Using this technique, the presented parametric study could be re-run allowing an accuracy check of the current one-dimensional model and providing a greater understanding of the forces at work. Modeling in three dimensions would also provide valuable information about the flame-heater combustion, allowing for a potentially more accurate combustion model to be generated, and helping designers develop more effective heaters.

BIBLIOGRAPHY

[1] Heywood, J.B., 1998, Internal Combustion Engine Fundamentals, McGraw-Hill, New York, p.34.

[2] Liu, H., Henein, N.A., and Bryzik, W., 2003, “Simulation of Diesel Engines Cold-Start,” SAE Paper 2003-01-0080.

[3] Polyakov,Y., and Valeev, D., 1992, “Diesel Fuel Heaters for Arctic Vehicles,” SAE Paper 920035.

[4] Solstad, L. G., 1966, “Cold Weather Starting Aids and Devices; Coolant, Battery, Lube Oil, Fuel Filter Heaters; Glow Plugs and Starting Fluid,” SAE Paper 660015.

[5] Zheng, J., Nichols, S., and Matthews, R., 1989, “Investigation of a Novel Aid for Cold Starting of Diesels,” SAE Paper 890041.

[6] Sukala, J. M., and Deckard, N., 1974, “Engine Heaters-First Aid for Cold Weather Starting,” SAE Paper 740549.

[7] Hakansson, N., Kemlin, J., and Nilsson, R., 1989, “Cold Starting the Volvo Way,” SAE Paper 890043.

[8] Payri F., Broatch, J.R., Serrano, L. F., and Esmoris, A., 2006, “Study of the Potential of Intake Air Heating in Automotive DI Diesel Engines,” SAE Paper 2006-01-1233.

[9] Lindl, B., and Schmitz, H., 1999, “Cold Start Equipment for Diesel Direct Injection Engines,” SAE Paper 1999-01-1244.

[10] Isley, W. F., 1964, “Development of Multifuel Features of the LD-465 and LDS-465 Military Engines,” SAE Paper 640371.

[11] L-3 Communications Combat Propulsion Systems. Advertisement. *AVDS-1790 750HP Engine*. L3 Communications, n.d. Web. 19 Mar. 2014. <http://www2.l-3com.com/cps/cps/750_hp.htm>.

[12] Gamma Technologies. *GT-SUITE Flow Theory Manual*. 7.1th ed. N.p.: Gamma Technologies, Inc., 2010. CD-ROM

[13] Tannehill, John C., Dale A. Anderson, and Richard H. Pletcher. *Computational Fluid Mechanics and Heat Transfer*. Second ed. Philadelphia: Taylor and Francis, 1997. Print.

[14] Kearney, Sean P., Anthony M. Jacobi, and Robert P. Lucht. "Time-Resolved Thermal Boundary-Layer Structure in a Pulsatile Reversing Channel Flow." *Journal of Heat Transfer* 123 (2001): 655-64. Web. 19 Mar. 2014.

[15] Habib, M A., S A. Said, A A. Al-Farayedhi, S A. Al-Dini, and A Asghar. "Heat transfer characteristics of pulsated turbulent pipe flow." *Heat and Mass Transfer* 34 (1999): 413-21. *Compendex*. Web. 1 Apr. 2014.

[16] US Department of Defense MIL-DTL83133G, 2010, “Turbine Fuels, Aviation, Kerosene Types, NATO F-34 (JP-8), NATO F-35 and JP-8+100.”

[17] Society of Automotive Engineers, 1983, “Handbook of Aviation Fuel Properties,” CRC Report No. 530.

[18] Edwards, T., 2003, “Liquid Fuels and Propellants for Aerospace Propulsion,” J. Propulsion and Power, 19(6), pp. 1089-1107.

[19] F. P. Incropera and D. P. DeWitt. Fundamentals of Heat and Mass Transfer. John Wiley and Sons, 1996, pp. 444-446.

[20] Molki, M., Sparrow, E. M. An empirical correlation for the average heat transfer coefficient in circular tubes. *Journal of Heat Transfer*, vol 108, 482, 1986

[21] Al-Arabi, M. "Turbulent Heat Transfer in the Entrance Region of a Tube." Heat Transfer Engineering 3.3-4 (1982): 76-83.

[22] Hausen, Helmuth. "Extended Equation for Heat Transfer in Tubes at Turbulent Flow; ERWEITERTE GLEICHUNG FUER DEN WAERMEUEBERGANG IN ROHREN BEI TURBULENTER STROEMUNG." Waerme- und Stoffuebertragung/Thermo- and Fluid Dynamics 7.4 (1974): 222-5.

[23] Söjberg, M., Dec, J. E., Hwang, W., 2007, “Thermodynamic and Chemical Effects of EGR and its Constituents on HCCI Autoignition,” SAE Paper 2007-01-0207.

[24] Ladommatos, N., Abdelhalim, S. M., Zhao, H., and Hu, Z., 1998, “Effects of EGR on Heat Release in Diesel Combustion,” SAE Paper 980184.

[25] Nitu, B., Singh, I., Zhong, L., Badreshany, K., Henein, N. A., and Bryzik, W., 2002, “Effect of EGR on Autoignition, Combustion, Regulated Emissions and Aldehydes in DI Diesel Engines,” SAE Paper 2002-01-1153.

[26] Olson, E. O. "Fuel Nozzles for Oil Burners." Delavan Documents. Delavan Inc., n.d. Web. 21 Feb. 2014.

APPENDIX A: PARAMETRIC STUDY CASE SUMMARY

Case	Period	DC	Maximum Temperature	Time to Maximum Temperature	Average Temperature	Total Fuel Used
1	4	0.2	533.2	29.1	451.4	14.8873
2	4	0.4	542.8	29.7	482.5	17.313301
3	4	0.6	542.6	29.3	501.7	18.8278
4	4	0.8	548.1	30	518.7	20.198599
5	5	0.2	531.5	26.3	441	13.9932995
6	5	0.4	540	27.13	475	16.636099
7	5	0.6	544	28.13	500.2	18.6504
8	5	0.8	547.1	29.13	517.4	20.059599
9	6	0.2	531.6	25.4	435.3	13.5353
10	6	0.4	536.1	25.4	469.3	16.1848
11	6	0.6	543.2	27.7	495.7	18.2779
12	6	0.8	547	29	517.1	20.032099
13	8	0.2	532	25.8	424.2	12.746401
14	8	0.4	538.6	27.4	463	15.753401
15	8	0.6	543.7	28.9	493.4	18.1674
16	8	0.8	547.7	30	515.4	19.939
17	10	0.2	528	22.2	400.8	10.9408
18	10	0.4	535.5	24.2	449.4	14.6222
19	10	0.6	541.2	26.2	486.2	17.506401
20	10	0.8	545.9	28.2	513	19.6707

APPENDIX B: INTAKE RUNNER GAS COMPOSITION RESULTS FOR PARAMETRIC STUDY

VALUES TAKEN AT END OF 30 SECONDS						
	Case 1					
	Runner 1	Runner 2	Runner 3	Runner 4	Runner 5	Runner 6
Unburned Air	0.673846	0.666749	0.666592	0.666653	0.666632	0.672457
Unburned Vapor Fuel	0.020646	0.019234	0.018411	0.018259	0.019032	0.020559
Unburned Liquid Fuel	0.005161	0.004808	0.004603	0.004565	0.004758	0.00514
O2	0.029548	0.032687	0.034411	0.03473	0.033111	0.029729
CO2	0.035019	0.03407	0.032802	0.03255	0.033774	0.035165
H2O	0.013675	0.013304	0.012808	0.01271	0.013188	0.013732
N2	0.223969	0.229544	0.230423	0.230499	0.22977	0.224983
CO	1.48E-06	1.39E-06	1.31E-06	1.29E-06	1.37E-06	1.49E-06
NO	4.16E-	4.44E-	4.57E-	4.59E-	4.48E-	4.18E-

	04	04	04	04	04	04
H2	3.42E-08	3.21E-08	3.01E-08	2.98E-08	3.16E-08	3.43E-08
N2 to combine into air	0.097266	0.107599	0.113276	0.114326	0.108995	0.097862
Remaining N2	0.126703	0.121945	0.117147	0.116173	0.120774	0.127121
New Unburned Air	0.80066	0.807035	0.81428	0.815709	0.808738	0.800047
Unburned Fuel (liq+vap)	0.025807	0.024042	0.023014	0.022824	0.02379	0.025698
Major Species (N2+H2O+CO2)	0.175397	0.169319	0.162757	0.161433	0.167737	0.176017
Minor Species (CO+NO+H2)	4.17E-04	4.46E-04	4.59E-04	4.61E-04	4.49E-04	4.20E-04
Fuel Injected in Cylinder	1.692	1.692	1.692	1.692	1.692	1.692
Effective A/F Ratio	31.02459	33.56777	35.38148	35.73964	33.99467	31.13234
Effective Equivalence Ratio	0.468983	0.433451	0.411232	0.407111	0.428008	0.46736
Major EGR	0.1753	0.1693	0.1627	0.1614	0.1677	0.1760

	97	19	57	33	37	17
Minor EGR	4.17E-04	4.46E-04	4.59E-04	4.61E-04	4.49E-04	4.20E-04
Effective A/F Ratio in Cylinder	5.770194	5.891087	5.988898	6.00783	5.914392	5.770311
Effective Equivalence Ratio in Cylinder	2.521579	2.469833	2.429495	2.421839	2.460101	2.521528

	Case 2					
	Runner1	Runner2	Runner3	Runner4	Runner5	Runner6
Unburned Air	0.671171	0.667383	0.667122	0.667097	0.667295	0.670605
Unburned Vapor Fuel	0.021092	0.021091	0.021079	0.021072	0.021088	0.021087
Unburned Liquid Fuel	0.005273	0.005273	0.00527	0.005268	0.005272	0.005272
O2	0.028785	0.028937	0.028967	0.028979	0.028945	0.028745
CO2	0.036115	0.03675	0.03678	0.036776	0.036761	0.036266
H2O	0.014103	0.014351	0.014363	0.014361	0.014355	0.014162
N2	0.224105	0.225928	0.226236	0.226432	0.225963	0.2243
CO	1.55E-06	1.58E-06	1.59E-06	1.59E-06	1.59E-06	1.56E-06
NO	4.12E-04	4.16E-04	4.16E-04	4.16E-04	4.16E-04	4.12E-04
H2	3.58E-08	3.66E-08	3.66E-08	3.66E-08	3.66E-08	3.60E-08

N2 to combine into air	0.094625	0.095255	0.095354	0.095393	0.095284	0.094625
Remaining N2	0.129675	0.130673	0.130881	0.131038	0.130679	0.129675
New Unburned Air	0.794541	0.791575	0.791443	0.791469	0.791524	0.793975
Unburned Fuel (liq+vap)	0.026359	0.026364	0.026349	0.02634	0.02636	0.026359
Major Species (N2+H2O+CO2)	0.180103	0.181774	0.182024	0.182176	0.181795	0.180103
Minor Species (CO+NO+H2)	4.14E-04	4.17E-04	4.18E-04	4.18E-04	4.17E-04	4.14E-04
Fuel Injected in Cylinder	1.692	1.692	1.692	1.692	1.692	1.692
Effective A/F Ratio	30.14288	30.02518	30.03658	30.04783	30.0273	30.1214
Effective Equivalence Ratio	0.482701	0.484593	0.484409	0.484228	0.484559	0.483045
Major EGR	0.180103	0.181774	0.182024	0.182176	0.181795	0.180103

Minor EGR	4.14E-04	4.17E-04	4.18E-04	4.18E-04	4.17E-04	4.14E-04
Effective A/F Ratio in Cylinder	5.703414	5.681936	5.681574	5.682129	5.681715	5.699351
Effective Equivalence Ratio in Cylinder	2.551103	2.560747	2.56091	2.56066	2.560846	2.552922

	Case 3					
	Runner1	Runner2	Runner3	Runner4	Runner5	Runner6
Unburned Air	0.668876	0.6672	0.66715	0.66715	0.667178	0.668812
Unburned Vapor Fuel	0.020943	0.020815	0.020762	0.020752	0.020802	0.020899
Unburned Liquid Fuel	0.005236	0.005204	0.005191	0.005188	0.0052	0.005225
O2	0.029149	0.0295	0.029609	0.029629	0.029527	0.029171
CO2	0.0363	0.036365	0.036293	0.036278	0.036349	0.036305
H2O	0.014175	0.0142	0.014172	0.014166	0.014194	0.014177
N2	0.225432	0.226349	0.226423	0.226431	0.226368	0.225386
CO	1.56E-06	1.55E-06	1.55E-06	1.55E-06	1.55E-06	1.56E-06

NO	4.16E-04	4.20E-04	4.21E-04	4.21E-04	4.20E-04	4.16E-04
H2	3.59E-08	3.59E-08	3.57E-08	3.57E-08	3.58E-08	3.59E-08
N2 to combine into air	0.095954	0.097108	0.097468	0.097534	0.097198	0.096025
Remaining N2	0.129478	0.129241	0.128955	0.128897	0.12917	0.129361
New Unburned Air	0.793979	0.793808	0.794226	0.794313	0.793903	0.794008
Unburned Fuel (liq+vap)	0.026179	0.026018	0.025953	0.025941	0.026002	0.026124
Major Species (N2+H2O+CO2)	0.179952	0.179807	0.179421	0.179341	0.179713	0.179843
Minor Species (CO+NO+H2)	4.18E-04	4.22E-04	4.22E-04	4.23E-04	4.22E-04	4.18E-04
Fuel Injected in Cylinder	1.692	1.692	1.692	1.692	1.692	1.692
Effective A/F Ratio	30.32931	30.50937	30.60269	30.62056	30.53207	30.39366
Effective Equivalence	0.479734	0.476903	0.475448	0.475171	0.476548	0.478718

Ratio						
Major EGR	0.179952	0.179807	0.179421	0.179341	0.179713	0.179843
Minor EGR	4.18E-04	4.22E-04	4.22E-04	4.23E-04	4.22E-04	4.18E-04
Effective A/F Ratio in Cylinder	5.706776	5.712118	5.71783	5.71896	5.713472	5.709217
Effective Equivalence Ratio in Cylinder	2.549601	2.547216	2.544672	2.544169	2.546613	2.54851

	Case 4					
	Runner1	Runner2	Runner3	Runner4	Runner5	Runner6
Unburned Air	0.667502	0.666986	0.666964	0.666962	0.666979	0.667813
Unburned Vapor Fuel	0.021077	0.021078	0.021078	0.021078	0.021078	0.021047
Unburned Liquid Fuel	0.005269	0.00527	0.005269	0.005269	0.00527	0.005262
O2	0.028932	0.028976	0.028978	0.028978	0.028976	0.028905
CO2	0.036734	0.0368	0.036803	0.036803	0.036801	0.036702
H2O	0.014345	0.01437	0.014371	0.014371	0.014371	0.014332

N2	0.225825	0.226092	0.226102	0.226103	0.226095	0.225586
CO	1.58E-06	1.59E-06	1.59E-06	1.59E-06	1.59E-06	1.58E-06
NO	4.15E-04	4.16E-04	4.16E-04	4.16E-04	4.16E-04	4.15E-04
H2	3.65E-08	3.66E-08	3.66E-08	3.66E-08	3.66E-08	3.65E-08
N2 to combine into air	0.095239	0.095383	0.09539	0.095391	0.095386	0.095149
Remaining N2	0.130586	0.130709	0.130712	0.130712	0.130709	0.130436
New Unburned Air	0.791672	0.791345	0.791332	0.791331	0.791341	0.791867
Unburned Fuel (liq+vap)	0.026346	0.026348	0.026347	0.026347	0.026348	0.026309
Major Species (N2+H2O+CO2)	0.181665	0.181879	0.181886	0.181886	0.181881	0.181471
Minor Species (CO+NO+H2)	4.17E-04	4.18E-04	4.18E-04	4.18E-04	4.18E-04	4.17E-04
Fuel Injected in Cylinder	1.692	1.692	1.692	1.692	1.692	1.692
Effective A/F Ratio	30.04944	30.03431	30.0348	30.03486	30.03447	30.09851

Effective Equivalence Ratio	0.484202	0.484446	0.484438	0.484437	0.484443	0.483413
Major EGR	0.181665	0.181879	0.181886	0.181886	0.181881	0.181471
Minor EGR	4.17E-04	4.18E-04	4.18E-04	4.18E-04	4.18E-04	4.17E-04
Effective A/F Ratio in Cylinder	5.68337	5.680923	5.680868	5.680863	5.680905	5.686258
Effective Equivalence Ratio in Cylinder	2.560101	2.561204	2.561228	2.561231	2.561212	2.5588

	Case 5					
	Runner1	Runner2	Runner3	Runner4	Runner5	Runner6
Unburned Air	0.674309	0.675389	0.675945	0.676034	0.675515	0.674824
Unburned Vapor Fuel	0.011777	0.010835	0.01044	0.010368	0.010749	0.011641
Unburned Liquid Fuel	0.002944	0.002709	0.00261	0.002592	0.002687	0.00291
O2	0.047979	0.049943	0.050741	0.050889	0.050116	0.04818

CO2	0.021062	0.019365	0.018655	0.018526	0.01921	0.020816
H2O	0.008221	0.007558	0.007281	0.007231	0.007498	0.008125
N2	0.233245	0.233697	0.233876	0.233896	0.233725	0.233035
CO	7.11E-07	6.39E-07	6.11E-07	6.06E-07	6.33E-07	7.01E-07
NO	5.44E-04	5.55E-04	5.60E-04	5.61E-04	5.56E-04	5.45E-04
H2	1.64E-08	1.47E-08	1.41E-08	1.40E-08	1.46E-08	1.62E-08
N2 to combine into air	0.157938	0.164405	0.167032	0.167519	0.164974	0.158601
Remaining N2	0.075306	0.069292	0.066844	0.066377	0.068751	0.074435
New Unburned Air	0.880226	0.889737	0.893718	0.894443	0.890605	0.881605
Unburned Fuel (liq+vap)	0.014722	0.013544	0.01305	0.01296	0.013437	0.014551
Major Species (N2+H2O+CO2)	0.104589	0.096215	0.09278	0.092134	0.095459	0.103376
Minor Species (CO+NO+H2)	5.44E-04	5.56E-04	5.60E-04	5.61E-04	5.57E-04	5.45E-04
Fuel Injected in Cylinder	1.692	1.692	1.692	1.692	1.692	1.692

Effective A/F Ratio	59.79172	65.69284	68.48173	69.01621	66.28094	60.58708
Effective Equivalence Ratio	0.243345	0.221485	0.212465	0.21082	0.21952	0.24015
Major EGR	0.104589	0.096215	0.09278	0.092134	0.095459	0.103376
Minor EGR	5.44E-04	5.56E-04	5.60E-04	5.61E-04	5.57E-04	5.45E-04
Effective A/F Ratio in Cylinder	6.894426	7.033801	7.092943	7.103799	7.046628	6.914458
Effective Equivalence Ratio in Cylinder	2.1104	2.068583	2.051335	2.0482	2.064817	2.104286

	Case 6					
	Runner1	Runner2	Runner3	Runner4	Runner5	Runner6
Unburned Air	0.67123	0.672532	0.673166	0.673271	0.672682	0.67182
Unburned Vapor Fuel	0.014181	0.012985	0.012482	0.012388	0.012873	0.013999

Unburned Liquid Fuel	0.003545	0.003246	0.00312	0.003097	0.003218	0.0035
O2	0.043067	0.045561	0.046589	0.046782	0.045789	0.043353
CO2	0.025369	0.023228	0.022329	0.022163	0.023027	0.025045
H2O	0.009904	0.009067	0.008716	0.008651	0.008989	0.009777
N2	0.232332	0.232958	0.23322	0.233241	0.233007	0.232119
CO	9.05E-07	8.05E-07	7.65E-07	7.58E-07	7.96E-07	8.90E-07
NO	5.14E-04	5.29E-04	5.36E-04	5.37E-04	5.31E-04	5.15E-04
H2	2.09E-08	1.86E-08	1.76E-08	1.75E-08	1.84E-08	2.05E-08
N2 to combine into air	0.14177	0.149981	0.153363	0.153998	0.15073	0.142712
Remaining N2	0.090562	0.082977	0.079857	0.079244	0.082277	0.089407
New Unburned Air	0.856067	0.868075	0.873117	0.874051	0.869202	0.857886
Unburned Fuel (liq+vap)	0.017726	0.016231	0.015602	0.015485	0.016092	0.017499
Major Species (N2+H2O+CO2)	0.125835	0.115272	0.110903	0.110058	0.114292	0.124229
Minor Species (CO+NO+H2)	5.15E-04	5.30E-04	5.36E-04	5.38E-04	5.32E-04	5.16E-04
Fuel Injected in Cylinder	1.692	1.692	1.692	1.692	1.692	1.692

Effective A/F Ratio	48.29525	53.48094	55.96059	56.44391	54.01577	49.02422
Effective Equivalence Ratio	0.301272	0.27206	0.260004	0.257778	0.269366	0.296792
Major EGR	0.125835	0.115272	0.110903	0.110058	0.114292	0.124229
Minor EGR	5.15E-04	5.30E-04	5.36E-04	5.38E-04	5.32E-04	5.16E-04
Effective A/F Ratio in Cylinder	6.55105	6.719778	6.791888	6.805345	6.735792	6.576367
Effective Equivalence Ratio in Cylinder	2.221018	2.16525	2.142261	2.138025	2.160102	2.212468

	Case 7					
	Runner1	Runner2	Runner3	Runner4	Runner5	Runner6
Unburned Air	0.667467	0.668996	0.669696	0.669823	0.669167	0.668155
Unburned Vapor Fuel	0.017394	0.015895	0.015258	0.015138	0.015747	0.01715
Unburned	0.004349	0.003974	0.003815	0.003784	0.003937	0.004288

Liquid Fuel						
O2	0.036497	0.039599	0.040906	0.041154	0.039902	0.036896
CO2	0.03106	0.028418	0.027296	0.027083	0.028156	0.036896
H2O	0.012127	0.011095	0.010656	0.010573	0.010993	0.011961
N2	0.230881	0.23173	0.23209	0.23212	0.231807	0.230641
CO	1.20E-06	1.06E-06	9.98E-07	9.87E-07	1.04E-06	1.18E-06
NO	4.72E-04	4.92E-04	5.01E-04	5.02E-04	4.94E-04	4.74E-04
H2	2.77E-08	2.44E-08	2.30E-08	2.28E-08	2.40E-08	2.72E-08
N2 to combine into air	0.120142	0.130353	0.134655	0.135473	0.13135	0.121456
Remaining N2	0.110739	0.101377	0.097435	0.096647	0.100457	0.109185
New Unburned Air	0.824105	0.838948	0.845257	0.84645	0.840419	0.826507
Unburned Fuel (liq+vap)	0.021743	0.019868	0.019073	0.018922	0.019683	0.021438
Major Species (N2+H2O+CO2)	0.153926	0.140891	0.135387	0.134304	0.139606	0.158041
Minor Species (CO+NO+H2)	4.73E-04	4.93E-04	5.02E-04	5.03E-04	4.95E-04	4.75E-04
Fuel Injected in Cylinder	1.692	1.692	1.692	1.692	1.692	1.692

Effective A/F Ratio	37.90226	42.22528	44.31796	44.73329	42.69679	38.55423
Effective Equivalence Ratio	0.383882	0.34458	0.328309	0.325261	0.340775	0.37739
Major EGR	0.153926	0.140891	0.135387	0.134304	0.139606	0.158041
Minor EGR	4.73E-04	4.93E-04	5.02E-04	5.03E-04	4.95E-04	4.75E-04
Effective A/F Ratio in Cylinder	6.118373	6.316475	6.402336	6.41869	6.336374	6.150148
Effective Equivalence Ratio in Cylinder	2.378083	2.3035	2.272608	2.266818	2.296266	2.365797

	Case 8					
	Runner1	Runner2	Runner3	Runner4	Runner5	Runner6
Unburned Air	0.667009	0.665877	0.665989	0.666069	0.665858	0.667205
Unburned Vapor Fuel	0.020905	0.019749	0.018988	0.018844	0.019564	0.020799
Unburned	0.005226	0.004937	0.004747	0.004711	0.004891	0.0052

Liquid Fuel						
O2	0.029259	0.031658	0.033236	0.033536	0.032042	0.029407
CO2	0.036592	0.035016	0.033806	0.033565	0.03473	0.036449
H2O	0.014289	0.013673	0.0132	0.013106	0.013562	0.014233
N2	0.226717	0.229292	0.230045	0.230127	0.229473	0.226871
CO	1.57E-06	1.45E-06	1.37E-06	1.35E-06	1.43E-06	1.56E-06
NO	4.18E-04	4.37E-04	4.49E-04	4.51E-04	4.40E-04	4.19E-04
H2	3.62E-08	3.35E-08	3.16E-08	3.12E-08	3.30E-08	3.60E-08
N2 to combine into air	0.096315	0.104213	0.109406	0.110394	0.105479	0.096802
Remaining N2	0.130402	0.125079	0.120638	0.119733	0.123994	0.130069
New Unburned Air	0.792582	0.801748	0.808631	0.809999	0.803379	0.793414
Unburned Fuel (liq+vap)	0.026131	0.024686	0.023736	0.023555	0.024455	0.025998
Major Species (N2+H2O+CO2)	0.181282	0.173768	0.167645	0.166403	0.172286	0.180752
Minor Species (CO+NO+H2)	4.20E-04	4.39E-04	4.50E-04	4.53E-04	4.42E-04	4.21E-04
Fuel Injected in Cylinder	1.692	1.692	1.692	1.692	1.692	1.692

Effective A/F Ratio	30.33055	32.4776	34.06835	34.38821	32.85186	30.51795
Effective Equivalence Ratio	0.479714	0.448001	0.427083	0.42311	0.442897	0.476769
Major EGR	0.181282	0.173768	0.167645	0.166403	0.172286	0.180752
Minor EGR	4.20E-04	4.39E-04	4.50E-04	4.53E-04	4.42E-04	4.21E-04
Effective A/F Ratio in Cylinder	5.698666	5.8251	5.915969	5.933832	5.846789	5.710113
Effective Equivalence Ratio in Cylinder	2.553229	2.497811	2.459445	2.452041	2.488545	2.548111

	Case 9					
	Runner1	Runner2	Runner3	Runner4	Runner5	Runner6
Unburned Air	0.676341	0.677231	0.677694	0.677769	0.677332	0.676823
Unburned Vapor Fuel	0.010277	0.009499	0.009167	0.009106	0.009428	0.010169
Unburned	0.002569	0.002375	0.002292	0.002277	0.002357	0.002542

Liquid Fuel						
O2	0.051032	0.052653	0.053325	0.053448	0.052796	0.051175
CO2	0.018362	0.016963	0.016366	0.016259	0.016835	0.018167
H2O	0.007167	0.00662	0.006387	0.006345	0.00657	0.00709
N2	0.233743	0.234133	0.234288	0.234311	0.234156	0.233526
CO	6.00E-07	5.46E-07	5.23E-07	5.19E-07	5.41E-07	5.92E-07
NO	5.61E-04	5.71E-04	5.74E-04	5.75E-04	5.72E-04	5.62E-04
H2	1.38E-08	1.26E-08	1.21E-08	1.20E-08	1.25E-08	1.37E-08
N2 to combine into air	0.16799	0.173327	0.175536	0.175942	0.173796	0.168461
Remaining N2	0.065753	0.060806	0.058751	0.05837	0.060361	0.065066
New Unburned Air	0.895363	0.903211	0.906555	0.907158	0.903923	0.896459
Unburned Fuel (liq+vap)	0.012847	0.011874	0.011458	0.011383	0.011785	0.012711
Major Species (N2+H2O+CO2)	0.091282	0.084389	0.081505	0.080974	0.083767	0.090323
Minor Species (CO+NO+H2)	5.62E-04	5.71E-04	5.75E-04	5.76E-04	5.72E-04	5.62E-04
Fuel Injected in Cylinder	1.692	1.692	1.692	1.692	1.692	1.692

Effective A/F Ratio	69.69589	76.06838	79.11684	79.69441	76.69808	70.52437
Effective Equivalence Ratio	0.208764	0.191275	0.183905	0.182572	0.189705	0.206312
Major EGR	0.091282	0.084389	0.081505	0.080974	0.083767	0.090323
Minor EGR	5.62E-04	5.71E-04	5.75E-04	5.76E-04	5.72E-04	5.62E-04
Effective A/F Ratio in Cylinder	7.117505	7.235858	7.286889	7.296164	7.246687	7.133892
Effective Equivalence Ratio in Cylinder	2.044256	2.010819	1.996737	1.994199	2.007814	2.03956

	Case 10					
	Runner1	Runner2	Runner3	Runner4	Runner5	Runner6
Unburned Air	0.673141	0.674332	0.674928	0.675023	0.674469	0.673684
Unburned Vapor Fuel	0.012638	0.01161	0.011179	0.0111	0.011516	0.012488
Unburned	0.003159	0.002902	0.002795	0.002775	0.002879	0.003122

Liquid Fuel						
O2	0.046228	0.048368	0.04924	0.049403	0.048558	0.046453
CO2	0.022611	0.020759	0.019985	0.019844	0.020589	0.022341
H2O	0.008826	0.008103	0.007801	0.007745	0.008037	0.008721
N2	0.232958	0.233442	0.233642	0.233662	0.233475	0.232741
CO	7.78E-07	6.98E-07	6.66E-07	6.60E-07	6.91E-07	7.67E-07
NO	5.33E-04	5.46E-04	5.51E-04	5.52E-04	5.47E-04	5.34E-04
H2	1.79E-08	1.61E-08	1.53E-08	1.52E-08	1.59E-08	1.77E-08
N2 to combine into air	0.152174	0.159221	0.162092	0.162628	0.159844	0.152915
Remaining N2	0.080784	0.074221	0.07155	0.071034	0.073631	0.079826
New Unburned Air	0.871542	0.88192	0.88626	0.887054	0.882871	0.873052
Unburned Fuel (liq+vap)	0.015797	0.014512	0.013974	0.013875	0.014395	0.01561
Major Species (N2+H2O+CO2)	0.112221	0.103084	0.099336	0.098623	0.102257	0.110889
Minor Species (CO+NO+H2)	5.34E-04	5.47E-04	5.52E-04	5.53E-04	5.48E-04	5.35E-04
Fuel Injected in Cylinder	1.692	1.692	1.692	1.692	1.692	1.692

Effective A/F Ratio	55.17181	60.77001	63.42126	63.93249	61.33121	55.92805
Effective Equivalence Ratio	0.263722	0.239427	0.229418	0.227584	0.237236	0.260156
Major EGR	0.112221	0.103084	0.099336	0.098623	0.102257	0.110889
Minor EGR	5.34E-04	5.47E-04	5.52E-04	5.53E-04	5.48E-04	5.35E-04
Effective A/F Ratio in Cylinder	6.769392	6.919029	6.98256	6.994291	6.932867	6.790965
Effective Equivalence Ratio in Cylinder	2.149381	2.102896	2.083763	2.080268	2.098699	2.142553

	Case 11					
	Runner1	Runner2	Runner3	Runner4	Runner5	Runner6
Unburned Air	0.66912	0.670685	0.671355	0.671471	0.670846	0.669925
Unburned Vapor Fuel	0.015829	0.014473	0.0139	0.013792	0.014343	0.015611
Unburned	0.003957	0.003618	0.003475	0.003448	0.003586	0.003903

Liquid Fuel						
O2	0.039717	0.042514	0.043689	0.043912	0.04278	0.040039
CO2	0.028306	0.025888	0.024871	0.02468	0.025656	0.027918
H2O	0.011051	0.010107	0.009709	0.009635	0.010016	0.0109
N2	0.231695	0.232358	0.232672	0.232697	0.232422	0.231363
CO	1.05E-06	9.29E-07	8.80E-07	8.71E-07	9.17E-07	1.03E-06
NO	4.93E-04	5.11E-04	5.18E-04	5.19E-04	5.12E-04	4.95E-04
H2	2.42E-08	2.14E-08	2.03E-08	2.01E-08	2.12E-08	2.38E-08
N2 to combine into air	0.130744	0.13995	0.143818	0.14455	0.140825	0.131801
Remaining N2	0.100951	0.092408	0.088854	0.088147	0.091596	0.099562
New Unburned Air	0.839582	0.853149	0.858862	0.859933	0.854452	0.841765
Unburned Fuel (liq+vap)	0.019787	0.018092	0.017375	0.01724	0.017929	0.019514
Major Species (N2+H2O+CO2)	0.140308	0.128403	0.123434	0.122462	0.127268	0.138379
Minor Species (CO+NO+H2)	4.94E-04	5.12E-04	5.19E-04	5.20E-04	5.13E-04	4.96E-04
Fuel Injected in Cylinder	1.692	1.692	1.692	1.692	1.692	1.692

Effective A/F Ratio	42.43163	47.15743	49.43205	49.87985	47.65828	43.13693
Effective Equivalence Ratio	0.342905	0.308541	0.294343	0.291701	0.305298	0.337298
Major EGR	0.140308	0.128403	0.123434	0.122462	0.127268	0.138379
Minor EGR	4.94E-04	5.12E-04	5.19E-04	5.20E-04	5.13E-04	4.96E-04
Effective A/F Ratio in Cylinder	6.325137	6.510493	6.590149	6.605177	6.528548	6.354649
Effective Equivalence Ratio in Cylinder	2.300345	2.234854	2.207841	2.202817	2.228673	2.289662

	Case 12					
	Runner1	Runner2	Runner3	Runner4	Runner5	Runner6
Unburned Air	0.66672	0.665943	0.666323	0.666435	0.666007	0.666743
Unburned Vapor Fuel	0.020611	0.019138	0.018366	0.018221	0.01895	0.020442
Unburned	0.005153	0.004785	0.004592	0.004555	0.004738	0.005111

Liquid Fuel						
O2	0.029847	0.032923	0.034522	0.034823	0.033312	0.030155
CO2	0.03621	0.034051	0.032772	0.032523	0.033746	0.035979
H2O	0.01414	0.013296	0.012796	0.012699	0.013177	0.014049
N2	0.227524	0.229925	0.230534	0.23059	0.230074	0.227822
CO	1.54E-06	1.39E-06	1.30E-06	1.29E-06	1.37E-06	1.52E-06
NO	4.23E-04	4.47E-04	4.58E-04	4.60E-04	4.50E-04	4.25E-04
H2	3.56E-08	3.20E-08	3.01E-08	2.97E-08	3.15E-08	3.52E-08
N2 to combine into air	0.098253	0.108376	0.11364	0.114633	0.109658	0.099267
Remaining N2	0.129271	0.121549	0.116894	0.115957	0.120417	0.128554
New Unburned Air	0.79482	0.807242	0.814485	0.815891	0.808977	0.796165
Unburned Fuel (liq+vap)	0.025764	0.023923	0.022958	0.022776	0.023688	0.025553
Major Species (N2+H2O+CO2)	0.179621	0.168896	0.162462	0.161179	0.167339	0.178582
Minor Species (CO+NO+H2)	4.25E-04	4.48E-04	4.60E-04	4.62E-04	4.51E-04	4.27E-04
Fuel Injected in Cylinder	1.692	1.692	1.692	1.692	1.692	1.692

Effective A/F Ratio	30.85013	33.7435	35.47764	35.82251	34.15148	31.15733
Effective Equivalence Ratio	0.471635	0.431194	0.410118	0.406169	0.426043	0.466985
Major EGR	0.179621	0.168896	0.162462	0.161179	0.167339	0.178582
Minor EGR	4.25E-04	4.48E-04	4.60E-04	4.62E-04	4.51E-04	4.27E-04
Effective A/F Ratio in Cylinder	5.729898	5.897722	5.9929	6.011284	5.920561	5.748333
Effective Equivalence Ratio in Cylinder	2.539312	2.467054	2.427873	2.420448	2.457537	2.531169

	Case 13					
	Runner1	Runner2	Runner3	Runner4	Runner5	Runner6
Unburned Air	0.675361	0.676347	0.67686	0.676943	0.676462	0.67586
Unburned Vapor Fuel	0.010998	0.010139	0.009776	0.00971	0.010061	0.010875
Unburned	0.002749	0.002535	0.002444	0.002428	0.002515	0.002719

Liquid Fuel						
O2	0.049566	0.051356	0.052089	0.052224	0.051514	0.04974
CO2	0.019659	0.018113	0.017461	0.017343	0.017972	0.019437
H2O	0.007673	0.007069	0.006815	0.006768	0.007014	0.007587
N2	0.233506	0.233923	0.234087	0.234109	0.233948	0.233293
CO	6.52E-07	5.90E-07	5.64E-07	5.60E-07	5.84E-07	6.43E-07
NO	5.53E-04	5.63E-04	5.68E-04	5.68E-04	5.64E-04	5.54E-04
H2	1.50E-08	1.36E-08	1.30E-08	1.29E-08	1.35E-08	1.48E-08
N2 to combine into air	0.163162	0.169056	0.171467	0.171912	0.169575	0.063984
Remaining N2	0.070343	0.064867	0.062619	0.062197	0.064373	-0.06398
New Unburned Air	0.888089	0.896759	0.900416	0.901078	0.89755	0.094295
Unburned Fuel (liq+vap)	0.013747	0.012674	0.01222	0.012138	0.012576	0.052459
Major Species (N2+H2O+CO2)	0.097676	0.090049	0.086895	0.086308	0.089359	0.176896
Minor Species (CO+NO+H2)	5.54E-04	5.64E-04	5.68E-04	5.69E-04	5.65E-04	#REF!
Fuel Injected in Cylinder	1.692	1.692	1.692	1.692	1.692	1.692

Effective A/F Ratio	64.60044	70.75754	73.68216	74.23916	71.37011	1.797505
Effective Equivalence Ratio	0.225231	0.205632	0.19747	0.195988	0.203867	8.094554
Major EGR	0.097676	0.090049	0.086895	0.086308	0.089359	0.176896
Minor EGR	5.54E-04	5.64E-04	5.68E-04	5.69E-04	5.65E-04	#REF!
Effective A/F Ratio in Cylinder	7.009492	7.138422	7.193498	7.20355	7.15028	0.570071
Effective Equivalence Ratio in Cylinder	2.075757	2.038265	2.02266	2.019837	2.034885	25.52315

	Case 14					
	Runner1	Runner2	Runner3	Runner4	Runner5	Runner6
Unburned Air	0.67051	0.67186	0.672516	0.672627	0.672017	0.671105
Unburned Vapor Fuel	0.014775	0.013512	0.012979	0.012879	0.013392	0.01458
Unburned	0.003694	0.003378	0.003245	0.00322	0.003348	0.003645

Liquid Fuel						
O2	0.041846	0.044485	0.045574	0.04578	0.044729	0.042163
CO2	0.026431	0.024172	0.023221	0.023045	0.023957	0.026083
H2O	0.010319	0.009436	0.009065	0.008996	0.009352	0.010183
N2	0.232078	0.232759	0.233042	0.233066	0.232813	0.231879
CO	9.56E-07	8.48E-07	8.05E-07	7.97E-07	8.38E-07	9.39E-07
NO	5.06E-04	5.23E-04	5.30E-04	5.31E-04	5.24E-04	5.08E-04
H2	2.21E-08	1.96E-08	1.86E-08	1.84E-08	1.93E-08	2.17E-08
N2 to combine into air	0.13775	0.146436	0.150023	0.150699	0.14724	0.138794
Remaining N2	0.094328	0.086322	0.083019	0.082367	0.085572	0.093085
New Unburned Air	0.850106	0.862781	0.868114	0.869105	0.863986	0.852062
Unburned Fuel (liq+vap)	0.018469	0.01689	0.016223	0.016099	0.01674	0.018225
Major Species (N2+H2O+CO2)	0.131078	0.11993	0.115305	0.114407	0.118881	0.129351
Minor Species (CO+NO+H2)	5.07E-04	5.24E-04	5.30E-04	5.32E-04	5.25E-04	5.09E-04
Fuel Injected in Cylinder	1.692	1.692	1.692	1.692	1.692	1.692

Effective A/F Ratio	46.02807	51.08298	53.51021	53.98542	51.61225	46.75148
Effective Equivalence Ratio	0.316111	0.284831	0.271911	0.269517	0.28191	0.31122
Major EGR	0.131078	0.11993	0.115305	0.114407	0.118881	0.129351
Minor EGR	5.07E-04	5.24E-04	5.30E-04	5.32E-04	5.25E-04	5.09E-04
Effective A/F Ratio in Cylinder	6.468624	6.644934	6.720505	6.734667	6.661904	6.495564
Effective Equivalence Ratio in Cylinder	2.249319	2.189638	2.165016	2.160463	2.18406	2.23999

	Case 15					
	Runner1	Runner2	Runner3	Runner4	Runner5	Runner6
Unburned Air	0.666467	0.666088	0.66665	0.666778	0.666211	0.666378
Unburned Vapor Fuel	0.020372	0.018732	0.017973	0.017829	0.018547	0.020162
Unburned	0.005093	0.004683	0.004493	0.004457	0.004637	0.005041

Liquid Fuel						
O2	0.030341	0.033767	0.035333	0.03563	0.034149	0.030759
CO2	0.03589	0.033387	0.032096	0.031847	0.033075	0.035595
H2O	0.014015	0.013036	0.012532	0.012435	0.012915	0.0139
N2	0.228135	0.23025	0.230775	0.230825	0.230375	0.228442
CO	1.52E-06	1.34E-06	1.26E-06	1.25E-06	1.32E-06	1.50E-06
NO	4.27E-04	4.53E-04	4.64E-04	4.66E-04	4.56E-04	4.30E-04
H2	3.50E-08	3.10E-08	2.91E-08	2.87E-08	3.05E-08	3.45E-08
N2 to combine into air	0.099878	0.111156	0.11631	0.117289	0.112412	0.101255
Remaining N2	0.128256	0.119094	0.114465	0.113536	0.117963	0.127187
New Unburned Air	0.796686	0.811011	0.818293	0.819697	0.812771	0.798393
Unburned Fuel (liq+vap)	0.025465	0.023415	0.022466	0.022287	0.023184	0.025203
Major Species (N2+H2O+CO2)	0.178161	0.165517	0.159093	0.157817	0.163953	0.176682
Minor Species (CO+NO+H2)	4.28E-04	4.54E-04	4.65E-04	4.67E-04	4.57E-04	4.32E-04
Fuel Injected in Cylinder	1.692	1.692	1.692	1.692	1.692	1.692

Effective A/F Ratio	31.28562	34.63638	36.42295	36.77953	35.05767	31.67902
Effective Equivalence Ratio	0.46507	0.420079	0.399473	0.3956	0.41503	0.459295
Major EGR	0.178161	0.165517	0.159093	0.157817	0.163953	0.176682
Minor EGR	4.28E-04	4.54E-04	4.65E-04	4.67E-04	4.57E-04	4.32E-04
Effective A/F Ratio in Cylinder	5.755758	5.94733	6.042762	6.061173	5.970355	5.77904
Effective Equivalence Ratio in Cylinder	2.527903	2.446476	2.407839	2.400525	2.437041	2.517719

	Case 16					
	Runner1	Runner2	Runner3	Runner4	Runner5	Runner6
Unburned Air	0.667148	0.666951	0.666951	0.666951	0.666951	0.667542
Unburned Vapor Fuel	0.021065	0.021077	0.021077	0.021077	0.021077	0.021039
Unburned	0.005266	0.005269	0.005269	0.005269	0.005269	0.00526

Liquid Fuel						
O2	0.028962	0.028979	0.028979	0.028979	0.028979	0.02893
CO2	0.036782	0.036804	0.036804	0.036804	0.036804	0.036737
H2O	0.014363	0.014372	0.014372	0.014372	0.014372	0.014346
N2	0.225971	0.226107	0.226107	0.226107	0.226107	0.22571
CO	1.59E-06	1.59E-06	1.59E-06	1.59E-06	1.59E-06	1.58E-06
NO	4.16E-04	4.16E-04	4.16E-04	4.16E-04	4.16E-04	4.15E-04
H2	3.66E-08	3.66E-08	3.66E-08	3.66E-08	3.66E-08	3.65E-08
N2 to combine into air	0.09534	0.095395	0.095395	0.095395	0.095395	0.095233
Remaining N2	0.130632	0.130712	0.130712	0.130712	0.130712	0.130477
New Unburned Air	0.79145	0.791324	0.791324	0.791324	0.791324	0.791705
Unburned Fuel (liq+vap)	0.026331	0.026347	0.026347	0.026347	0.026347	0.026299
Major Species (N2+H2O+CO2)	0.181777	0.181889	0.181889	0.181889	0.181889	0.18156
Minor Species (CO+NO+H2)	4.18E-04	4.18E-04	4.18E-04	4.18E-04	4.18E-04	4.17E-04
Fuel Injected in Cylinder	1.692	1.692	1.692	1.692	1.692	1.692

Effective A/F Ratio	30.05802	30.03512	30.03512	30.03512	30.03512	30.10448
Effective Equivalence Ratio	0.484064	0.484433	0.484433	0.484433	0.484433	0.483317
Major EGR	0.181777	0.181889	0.181889	0.181889	0.181889	0.18156
Minor EGR	4.18E-04	4.18E-04	4.18E-04	4.18E-04	4.18E-04	4.17E-04
Effective A/F Ratio in Cylinder	5.682385	5.680833	5.680833	5.680833	5.680833	5.685529
Effective Equivalence Ratio in Cylinder	2.560544	2.561244	2.561244	2.561244	2.561244	2.559129

	Case 17					
	Runner1	Runner2	Runner3	Runner4	Runner5	Runner6
Unburned Air	0.680655	0.68056	0.680458	0.680425	0.680553	0.680958
Unburned Vapor Fuel	0.005991	0.005165	0.004738	0.004656	0.005082	0.005904
Unburned	0.001498	0.001291	0.001184	0.001164	0.00127	0.001476

Liquid Fuel						
O2	0.059954	0.061851	0.06284	0.063033	0.06204	0.060083
CO2	0.01078	0.009351	0.008617	0.008476	0.009209	0.010628
H2O	0.004205	0.003647	0.003361	0.003306	0.003592	0.004146
N2	0.236556	0.237904	0.238728	0.238875	0.238042	0.236443
CO	3.26E-07	2.79E-07	2.55E-07	2.51E-07	2.74E-07	3.21E-07
NO	6.12E-04	6.23E-04	6.29E-04	6.30E-04	6.24E-04	6.12E-04
H2	7.51E-09	6.43E-09	5.88E-09	5.78E-09	6.32E-09	7.40E-09
N2 to combine into air	0.19736	0.203605	0.206859	0.207495	0.204226	0.197784
Remaining N2	0.039196	0.034299	0.03187	0.03138	0.033815	0.038659
New Unburned Air	0.937969	0.946016	0.950157	0.950952	0.946819	0.938825
Unburned Fuel (liq+vap)	0.007489	0.006456	0.005922	0.00582	0.006352	0.00738
Major Species (N2+H2O+CO2)	0.054181	0.047298	0.043847	0.043162	0.046616	0.053433
Minor Species (CO+NO+H2)	6.12E-04	6.23E-04	6.29E-04	6.30E-04	6.24E-04	6.13E-04
Fuel Injected in Cylinder	1.692	1.692	1.692	1.692	1.692	1.692

Effective A/F Ratio	125.243	146.5406	160.4474	163.4033	149.0504	127.2139
Effective Equivalence Ratio	0.116174	0.09929	0.090684	0.089044	0.097618	0.114374
Major EGR	0.054181	0.047298	0.043847	0.043162	0.046616	0.053433
Minor EGR	6.12E-04	6.23E-04	6.29E-04	6.30E-04	6.24E-04	6.13E-04
Effective A/F Ratio in Cylinder	7.787864	7.922668	7.993072	8.006652	7.936256	7.802051
Effective Equivalence Ratio in Cylinder	1.868292	1.836503	1.820326	1.817239	1.833358	1.864894

	Case 18					
	Runner1	Runner2	Runner3	Runner4	Runner5	Runner6
Unburned Air	0.678741	0.679278	0.679579	0.679631	0.679341	0.67912
Unburned Vapor Fuel	0.008503	0.00786	0.007563	0.007509	0.007799	0.008423
Unburned	0.002126	0.001965	0.001891	0.001877	0.00195	0.002106

Liquid Fuel						
O2	0.054631	0.056	0.056615	0.056727	0.056125	0.054729
CO2	0.015181	0.014039	0.013516	0.013421	0.013933	0.015039
H2O	0.005924	0.005478	0.005274	0.005237	0.005437	0.005869
N2	0.234372	0.234882	0.235094	0.235132	0.234917	0.234198
CO	4.80E-07	4.38E-07	4.20E-07	4.16E-07	4.34E-07	4.74E-07
NO	5.82E-04	5.89E-04	5.93E-04	5.94E-04	5.90E-04	5.82E-04
H2	1.11E-08	1.01E-08	9.67E-09	9.60E-09	1.00E-08	1.09E-08
N2 to combine into air	0.179836	0.184343	0.186368	0.186737	0.184754	0.180159
Remaining N2	0.054536	0.050538	0.048726	0.048395	0.050163	0.054039
New Unburned Air	0.913207	0.919621	0.922563	0.923095	0.92022	0.914008
Unburned Fuel (liq+vap)	0.010629	0.009825	0.009454	0.009387	0.009749	0.010529
Major Species (N2+H2O+CO2)	0.075642	0.070056	0.067516	0.067054	0.069532	0.074947
Minor Species (CO+NO+H2)	5.82E-04	5.90E-04	5.93E-04	5.94E-04	5.91E-04	5.82E-04
Fuel Injected in Cylinder	1.692	1.692	1.692	1.692	1.692	1.692

Effective A/F Ratio	85.91717	93.60361	97.58426	98.33979	94.38858	86.80602
Effective Equivalence Ratio	0.169349	0.155443	0.149102	0.147956	0.15415	0.167615
Major EGR	0.075642	0.070056	0.067516	0.067054	0.069532	0.074947
Minor EGR	5.82E-04	5.90E-04	5.93E-04	5.94E-04	5.91E-04	5.82E-04
Effective A/F Ratio in Cylinder	7.389633	7.490282	7.536994	7.545486	7.499762	7.402075
Effective Equivalence Ratio in Cylinder	1.968975	1.942517	1.930478	1.928305	1.940061	1.965665

	Case 19					
	Runner1	Runner2	Runner3	Runner4	Runner5	Runner6
Unburned Air	0.674308	0.675437	0.675976	0.676062	0.675559	0.674872
Unburned Vapor Fuel	0.011731	0.01081	0.010424	0.010353	0.010727	0.011602
Unburned	0.002933	0.002702	0.002606	0.002588	0.002682	0.0029

Liquid Fuel						
O2	0.048089	0.049994	0.050773	0.050918	0.05016	0.048263
CO2	0.020977	0.019318	0.018625	0.018499	0.019169	0.020744
H2O	0.008188	0.00754	0.007269	0.00722	0.007482	0.008097
N2	0.233305	0.233696	0.233872	0.233891	0.233724	0.233049
CO	7.08E-07	6.37E-07	6.10E-07	6.05E-07	6.31E-07	6.98E-07
NO	5.44E-04	5.56E-04	5.60E-04	5.61E-04	5.57E-04	5.45E-04
H2	1.63E-08	1.47E-08	1.41E-08	1.39E-08	1.46E-08	1.61E-08
N2 to combine into air	0.158301	0.164571	0.167137	0.167613	0.165119	0.158873
Remaining N2	0.075004	0.069125	0.066735	0.066278	0.068605	0.074175
New Unburned Air	0.880697	0.890002	0.893887	0.894593	0.890837	0.882008
Unburned Fuel (liq+vap)	0.014664	0.013512	0.01303	0.012942	0.013409	0.014502
Major Species (N2+H2O+CO2)	0.10417	0.095983	0.092629	0.091997	0.095256	0.103016
Minor Species (CO+NO+H2)	5.45E-04	5.56E-04	5.61E-04	5.61E-04	5.57E-04	5.46E-04
Fuel Injected in Cylinder	1.692	1.692	1.692	1.692	1.692	1.692

Effective A/F Ratio	60.05902	65.86774	68.60195	69.12499	66.43696	60.81992
Effective Equivalence Ratio	0.242262	0.220897	0.212093	0.210488	0.219005	0.239231
Major EGR	0.10417	0.095983	0.092629	0.091997	0.095256	0.103016
Minor EGR	5.45E-04	5.56E-04	5.61E-04	5.61E-04	5.57E-04	5.46E-04
Effective A/F Ratio in Cylinder	6.901235	7.037669	7.095428	7.106023	7.050031	6.920282
Effective Equivalence Ratio in Cylinder	2.108318	2.067446	2.050616	2.047559	2.063821	2.102515

	Case 20					
	Runner1	Runner2	Runner3	Runner4	Runner5	Runner6
Unburned Air	0.667392	0.669002	0.669703	0.669829	0.669173	0.668069
Unburned Vapor Fuel	0.017374	0.015883	0.015251	0.015131	0.015737	0.017134
Unburned	0.004344	0.003971	0.003813	0.003783	0.003934	0.004284

Liquid Fuel						
O2	0.036546	0.039623	0.040921	0.041167	0.039922	0.036942
CO2	0.031037	0.028399	0.027283	0.027072	0.028139	0.030615
H2O	0.012118	0.011088	0.010652	0.010569	0.010986	0.011953
N2	0.230941	0.231737	0.232091	0.23212	0.231813	0.230707
CO	1.20E-06	1.05E-06	9.97E-07	9.87E-07	1.04E-06	1.18E-06
NO	4.72E-04	4.92E-04	5.01E-04	5.02E-04	4.94E-04	4.74E-04
H2	2.77E-08	2.43E-08	2.30E-08	2.28E-08	2.40E-08	2.72E-08
N2 to combine into air	0.120304	0.130431	0.134704	0.135517	0.131419	0.121607
Remaining N2	0.110637	0.101306	0.097387	0.096604	0.100394	0.1091
New Unburned Air	0.824242	0.839056	0.845327	0.846513	0.840515	0.826618
Unburned Fuel (liq+vap)	0.021718	0.019854	0.019064	0.018914	0.019671	0.021418
Major Species (N2+H2O+CO2)	0.153792	0.140792	0.135321	0.134244	0.139519	0.151668
Minor Species (CO+NO+H2)	4.73E-04	4.93E-04	5.02E-04	5.03E-04	4.95E-04	4.75E-04
Fuel Injected in Cylinder	1.692	1.692	1.692	1.692	1.692	1.692

Effective A/F Ratio	37.95197	42.2609	44.34255	44.75537	42.72869	38.5954
Effective Equivalence Ratio	0.383379	0.34429	0.328127	0.325101	0.340521	0.376988
Major EGR	0.153792	0.140792	0.135321	0.134244	0.139519	0.151668
Minor EGR	4.73E-04	4.93E-04	5.02E-04	5.03E-04	4.95E-04	4.75E-04
Effective A/F Ratio in Cylinder	6.12052	6.317967	6.403308	6.419554	6.337691	6.15189
Effective Equivalence Ratio in Cylinder	2.377249	2.302956	2.272263	2.266513	2.295789	2.365127

APPENDIX C: SCRIPT FOR CALCULATING NOZZLE FLOW RATE

```
t=[0:.05:9];
rise=[0.5616*t];
fall=-.0016.*t.^3+.0252.*t.^2-.1754.*t+.7067;
gttime=transpose([0:.05:30]);

dc=.8;
p=10;

end1=p*dc/.05+1;
end2=p*1/.05;

for n=[1:1:end1]
if n<26
m(n)=rise(n+1);
else
m(n)=0.702;
end
end

[throw,ind]=min(abs(m(n)-fall));
s=ind-n;
for n=[end1+1:1:end2]
if n<200-(ind-2)
m(n)=fall(s+n);
else
m(n)=0;
end
end

gtm=[transpose([.05:.05:p]) transpose(m)];
```